SETTLING OF POROUS SPHERES, AS A PROXY FOR MARINE SNOW, THROUGH DENSITY STRATIFICATION

Sungduk Yu

A thesis submitted to the faculty of the University of North Carolina at Chapel Hill in partial fulfillment of the requirements for the degree of Master of Science in the Department of Marine Sciences.

Chapel Hill
2013

Approved by:

Brian L. White

Carol Arnosti

John M. Bane

Richard M. McLaughlin

Harvey E. Seim

Abstract

SUNGDUK YU: Settling of porous spheres, as a proxy for marine snow, through density stratification
(Under the direction of Brian L. White.)

The settling of marine snow, which is a dominant form of settling particulate organic carbon (POC), is a major pathway for carbon transport from the surface to the deep ocean. Although there have been many studies to estimate the global POC flux, the physical settling behavior of POC at an individual level has not been well investigated. Because marine snow is a hotspot for microbial activity, most POC is remineralized while sinking through the upper water column, limiting the total carbon export to the deep ocean. Thus, an understanding of the competing timescales of physical sinking vs. remineralization can lead to a better understanding of vertical carbon flux. Accordingly, the time scale of delayed settling of porous particles at the stratified region (residence time, τ_r) is the key variable in this study. Here we present experimental results for the settling of a single and a cloud of porous spheres, as a proxy for marine snow, through water columns with various stratification regimes, e.g. homogeneous, 2-layered, and linearly stratified. In addition, the experimental results were compared with the results from numerical models formulated both for a single and a cloud of spheres. We found that the settling of porous spheres can be characterized by two regimes depending on their sizes—when sphere sizes are small, their settling behavior at a density interface is governed by their settling rate (settling regime), and when sphere sizes are large, their settling behavior at a density interface is governed by molecular diffusion (diffusion regime). In the settling regime, τ_r decreases with sphere size, while in the diffusion regime, τ_r increases with sphere size. The numerical models could predict the overall tendency of τ_r over the sphere sizes (e.g. the settling and diffusion regimes), but the τ_r from the numerical models were underestimated compared to the laboratory experimental results. However, the modified numerical model, which included the entrained fluid shell around a sphere, was able to return τ_r similar to the laboratory experimental results. Considering that the thin layers in the ocean are usually observed near density discontinuities, the prolonged retention of porous spheres within density stratification we observed could be a possible mechanism of thin layer formation.

ACKNOWLEDGMENTS

Many people have helped me along the way of my research. First of all, I should like to convey my big thanks to Brian White, my advisor, who gave me an opportunity to be here together with UNC's Marine Sciences department and complete my master's research and who I discussed with about my research the most. I also had invaluable feedbacks on my research from my committee members (most of them were my class teachers, too)—Carol Arnosti, John Bane, Richard McLaughlin, and Harvey Seim—and from CMG project team—Roberto Camassa, Claudia Falcon, Emma He, Shilpa Khatri, Jenny Prairie, Chung-nan Tzou, and Bailey Watson. Also, Rachel Copeland and Lindsay Leonard helped me not miss the important time line. I also want to thank all my friends at UNC, who made this land home. I owe you more than I can return. To name a few, Elaine Monburu, Anna Jalowska, Tingting Yang, Jenny Prairie, Ivana Vu, Winnie Yu, Jihyuk Kim, Luke McKay, JP Balmonte, Popo, Jamie Browne, Sarah Underwood, Jesse Bikman, Natalie Cohen, Lisa Nigro, Ben Von Korff, Caroline Lowcher, Luke Dodd, Dan Hoer, and Mike Muglia (he surfs). Also, I thank my friends at home for moral support. Eunkyu Park, EJ Choi, Now He Sung, Juhnghwa Lee, Byungho Cha, and Byungjun Song. Ultimately, my family. Thank you always for your unconditional support and love. (This work has been financially supported by National Science Foundation CMG Program ARC-1025523 and the Department of Marine Sciences at UNC Chapel Hill)

Contents

List of Tables

Table

List of Figures

Figure

Chapter 1

Background

Settling of marine snow, organic aggregates larger than 0.5 mm in diameter (Alldredge & Silver 1988) and a dominant form of settling particulate organic carbon (POC) (Fowler & Knauer 1986), has a central role in transporting organic carbon from the surface ocean to the interior ocean (Turner 2002). This has a direct linkage to the climate, for example, Falkowski (2000) estimated the annual export of 11–16 Gt of organic carbon from the surface to the deep ocean makes atmospheric carbon dioxide concentration 150–200 ppmv lower than the case with no primary production in the ocean. However, estimating how much organic carbon is exported is uncertain due to imperfect existing methodologies and limited sampled data (Burd *et al.* 2010). Studies using sediment traps, the only tool which can directly measure POC flux, gave 5.36 GtC/yr of global export production (Honjo *et al.* 2008). The model calculation based on the empirical relationship between sea surface temperature (SST), net primary production, and export production gave 11.1–20.9 GtC/yr depending on the model algorithms (Laws *et al.* 2000). An alternative approach using relationship between ^{234}Th–^{238}U and SST yielded about 5 GtC/yr (Henson *et al.* 2011). In contrast to many efforts to estimate the global POC flux, the physical settling process of individual POCs has been left largely unstudied. The better understanding of the physical settling processes mechanistically will contribute the better incorporation of field data and important biogeochemical processes to the model. Accordingly, it will lead to the better estimation of the global POC flux.

A handful of studies in the lab as well as the field have been done on the settling rate of marine particulates such as fecal pellets, marine snows, and phytoplankton. Turner (2002) authored a review on the topic, and a summary of his review is given in table 1. The settling velocity of marine snow spans a wide range (16–368 m/day) because of variation in its density, size, and morphology. The settling velocity of marine snow has been found to increase with its size by lab experiments and in situ measurements (Kajihara 1971; Alldredge & Gotschalk 1988; Iversen & Ploug 2010), and porosity also increases with the size (Kajihara 1971; Alldredge &

Gotschalk 1988). Iversen & Ploug (2010) found the excess density of marine snow to the ambient water decreases with its size, while Alldredge & Gotschalk (1988) found no correlation between them. Besides the experimental studies, models to predict settling velocity and excess density of flocculated sediment in the river and coastal environment were proposed (Kranenburg 1994; Khelifa & Hill 2006).

Particles	Sinking rate ($m\ d^{-1}$)	Source
Fecal pellets of:		
Copepods	5–220	Smayda (1971), Turner (1977), Honjo & Roman (1978), Paffenhöfer & Knowles (1979), Small et al. (1979), Bienfang (1980), Yoon et al. (2001)
Euphausiids	16–862	Fowler & Small (1972), Youngbluth et al. (1989), Yoon et al. (2001)
Doliolids	41–504	Bruland & Silver (1981), Deibel (1990)
Appendicularians	25–166	Gorsky et al. (1984)
Chaetognaths	27–1313	Dilling & Alldredge (1983)
Pteropods	120–1800	Bruland & Silver (1981), Yoon et al. (2001)
Heteropods	120–646	Yoon et al. (2001)
Salps	43–2700	Madin (1982), Yoon et al. (2001)
Marine snow	16–368	Alldredge (1979), Shanks & Trent (1980), Silver & Alldredge (1981), Taguchi (1982b), Gorsky et al. (1984), Asper (1987), Alldredge & Gotschalk (1988)
Phytodetritus	100–150	Billett et al. (1983), Lampitt (1985)

Table 1: Sinking rates of zooplankton fecal pellets, marine snow and phytodetritus(adapted from Turner 2002).

Regardless of whether they were experimental or in situ observational studies, the previous studies were not able to actively control the important parameters of marine snows including size, density, porosity, and shape. Considering the various origins of marine snow, ones with an identical size and shape do not necessarily have same properties. Accordingly, a systematic approach is desired to elucidate the underlying physical processes.

Another limitation of the previous studies is that the majority of them examined settling velocities in a homogeneous density water column, not in a stratified environment, which is an ubiquitous feature of the ocean. In the tropics and temperate regions, the thermocline is a permanent feature of water column. The polar region generally lacks a permanent thermocline, but a seasonal thermocline often exists, and density stratification is also driven by salinity difference due to ice melting and formation. In addition to the bulk stratification, multiple pycnoclines at a meter scale in the surface ocean exist (Prairie *et al.* 2010). These density discontinuities have a significant correlation with marine snow's vertical distribution (MacIntyre *et al.* 1995;

Dekshenieks *et al.* 2001; McManus *et al.* 2008; Prairie *et al.* 2010).

Lastly, the studies based on an individual particle overlook possible interactions between particles. This issue will be especially important for the episodic settling of large numbers of particles, e.g. algal blooms.

Only a very few studies have investigated the effect of stratification on the settling of real marine particles or porous particles. MacIntyre *et al.* (1995) studied the vertical distribution of marine snow and its correlation with density discontinuities by analyzing observational data and using models. Kindler *et al.* (2010) used manufactured porous particles and they found the porous particles are trapped for some period of time at the density transition layer to exchange the interstitial and the ambient fluids by molecular diffusion. Prairie *et al.* (2012) conducted similar research to Kindler *et al.* (2010) but with natural aggregates and proposed two possible mechanisms which reduce the settling velocity of particles in the density interface: 1) by diffusion, which is also observed by Kindler *et al.* (2010), and 2) by entrainment of lighter fluid from the upper layer.

In this study, the settling behavior of a single and a cloud of porous spheres, which resembles the highly porous nature of marine snow, was investigated. By using manufactured porous spheres, the key factors could be studied systematically because of the exclusion of the variability and uncertainty of physical characteristics including porosity, solid matrix density, and shape. In *Theory*, the governing physics will be discussed. In *Methods*, the experimental procedure and the formulation of the numerical model will be introduced. In *Results* and *Discussion*, the results from laboratory experiment and numerical simulation will be presented and discussed. Finally, in *Conclusions*, the findings of this study will be summarized, and future work will be suggested.

Theory

The porosity of spheres and the presence of density stratification distinguish this study from previous studies. The initial density of porous particles in this study is always lighter than the bottom layer (BL) fluid, while it is heavier than the top layer (TL) fluid. Once a porous particle reaches the depth of its neutral density, its settling speed is significantly reduced, and it gains further negative buoyancy by diffusive exchange of lighter interstitial fluid with denser ambient fluid. This density adjustment is unique to porous particles.

Settling of a single porous sphere in a stratified water column

The settling of a low Reynolds number sphere is governed by the Basset-Boussinesq-Oseen (BBO) equation. When no ambient fluid motion exists, the BBO equation is expressed as

$$\frac{\pi}{6}\rho_s d^3\frac{dU}{dt} = -\frac{\pi}{8}\rho_f U^2 C_D d^2 - \frac{\pi}{12}\rho_f d^3\frac{dU}{dt} - \frac{3}{2}d^2\sqrt{\pi\rho_f\mu}\int_{t_0}^{t}\frac{1}{\sqrt{t-\tau}}\frac{dU}{d\tau}\,d\tau + \frac{\pi}{6}(\rho_s-\rho_f)d^3 g \quad (1)$$

where ρ_s is the density of the sphere, d is the diameter of the sphere, U is the settling velocity of the sphere, ρ_f is the density of the ambient fluid, t is time, C_D is drag coefficient, μ is dynamic viscosity of a fluid, and g is gravity (modified from Johnson 1998, chapter 18). The term on the left hand side is inertia, and the terms on the right hand side are drag force, added mass effect, basset force, and reduced gravity, respectively. In this study, the added mass effect and basset force are negligible (Khatri, 2012, unpublished data). Hence, equation (1) is simplified to

$$\frac{\pi}{6}\rho_s d^3\frac{dU}{dt} = -\frac{\pi}{8}\rho_f U^2 C_D d^2 + \frac{\pi}{6}(\rho_s-\rho_f)d^3 g\,. \quad (2)$$

As the Reynolds numbers of the spheres ranges from 0.1 to 10 in this study, a corrected Stokes drag law was used (White 1974):

$$C_D = \frac{24}{Re} + \frac{6}{1+\sqrt{Re}} + 0.4 \quad (3)$$

$$(Re = \frac{\rho_f U d}{\mu}).$$

For a stratified water column, ρ_f is not a constant but a function of depth, z,

$$\rho_f = \rho_f(z).$$

Accordingly, while a sphere is sinking, ρ_s also changes over time since diffusive exchange occurs whenever a density difference exists between ambient fluid and the interstitial fluid of a porous sphere. The density of a porous sphere with a porosity, P, which is a volume fraction of the interstitial fluid out of the total volume of the sphere, can be defined as

$$\rho_s = P\rho_{f'} + (1-P)\rho_m \quad (4)$$

where $\rho_{f'}$ is the average density of interstitial fluid, and ρ_m is the solid matrix density. Here, $\rho_{f'}$ is theoretically a function of temperature, the concentration of salt inside a sphere, and pressure. Assuming the fluid is incompressible and temperature is constant, $\rho_{f'}$ becomes a function of only

salt concentration, C:

$$\rho_{f'} = \rho_{f'}(C).$$

C of the interstitial fluid of a sphere can change in a stratified water column, whenever a concentration difference exists between the ambient fluid and the interstitial fluid of the sphere. The salt concentration of the ambient fluid, C_f at the surface of a sphere, which changes over time while a sphere is settling through stratification, drives molecular diffusion of salt into the sphere. Also, the gradient of salt inside a sphere usually exists because diffusion is a slow process compared to sinking of a sphere:

$$C = C(r, t)$$

where r is the distance from the center to a point in a sphere.

The diffusive process can be described by Fick's second law, assuming diffusion coefficient, D, is a constant.

$$\frac{\partial C}{\partial t} = \frac{D}{r^2}\frac{\partial}{\partial r}(r^2\frac{\partial C}{\partial r}) \tag{5}$$

Initial condition: $C(r, 0) = 0$

Boundary conditions: $\partial c/\partial r = 0$ at $r = 0$, and $C = C_f$ at $r = d/2$

Then, the average concentration of interstitial fluid inside a sphere can be calculated.

$$C_{avg}(t) = \frac{\int_0^{d/2} C(r,t)\,\pi r^2 dr}{\frac{1}{6}\pi d^3} \tag{6}$$

$$\rho_{f'} = \rho_{f'}(c_{avg})$$

In this study, sodium chloride (NaCl) was used to stratify a water column. The conversion between $\rho_{f'}$ and [NaCl] was interpolated using a density-concentration table at $20°C$ (in appendix, Mettler Toledo).

Settling of a cloud of porous spheres in a stratified water column

If multiple particles settle simultaneously, the settling behavior of each particle might be different from the case of a single particle settling. For example, a particle cloud—a mixture of particles and fluid, the total density of which is higher than that of water column to be released—released instantaneously at the top of water column of homogeneous fluid descend in a form of thermal (hereafter, a negatively buoyant fluid mass will be called a thermal). Due to turbulent entrainment, the width of the thermal increases and the settling speed decreases as it sinks and incorporates the ambient fluid (Scorer 1957). Accordingly, the control factors determining the growth of a thermal can be described by its vertical location from the origin

and the total buoyancy, Q,

$$Q = g'V_0,$$

where Q is the released total buoyancy, g' ($= \frac{\rho-\rho_f}{\rho}g$) is the reduced gravity, ρ and V_0 are the initial density and the volume of the thermal, ρ_f is the density of the ambient fluid, and V is the volume of the thermal. Then, dimensional study shows

$$b = c_1 z, \qquad W = c_2 Q^{1/2}/z, \qquad g' = c_3 Q/z^3,$$

where b is the half horizontal length of the thermal, z is the vertical length of the front from the release point, and W is the settling speed of the thermal (Noh & Fernando 1993; Bush *et al.* 2003). The constants (c_1, c_2, and c_3) can be obtained empirically.

In a homogeneous column, theoretically the thermal, which consists only of a fluid denser than the water column, can sink indefinitely satisfying the above similarity condition because it has excess negative buoyancy at any moment. However, a particle cloud, which consists of heavy particles and a fluid with density identical to that of the water column, initially forms a thermal but does not propagate indefinitely. At a certain point, the particles in the thermal will fall out, and the separated particles form a bowl-shaped cluster, which settles as a group of independent individual particle, not as a thermal (Slack 1963; Rahimipour & Wilkinson 1992; Bühler & Papantoniou 2001; Noh & Fernando 1993; Bush *et al.* 2003). Accordingly, two different regimes exist: the so called *thermal regime* and the *particle settling regime* (Noh & Fernando 1993). Noh & Fernando's (1993) experiment found the critical depth measured from a virtual origin, z_c, where the transition between the two regimes happens, follows the relationship, $z_c w_s/\nu \sim (q/\nu w_s)^\alpha$ with $\alpha \simeq 0.3$, where w_s is the terminal settling velocity of an individual particle, ν is kinematic viscosity, and q ($= \frac{4}{3}\pi a^3 g' N$ where a and ρ_p are the radius and the density of a particle, respectively, g' is the reduced gravity of the particles, $\frac{\rho_p-\rho_f}{\rho_p}g$, and N is the number of the released particles per unit length) is the total buoyancy of the released particles per unit length. Later, Bush *et al.* (2003) found another empirical relationship: $z_c/a = (11 \pm 2)(Q^{1/2}/w_s a)^{5/6}$.

Compared to a cloud of particles in a homogeneous environment, the settling of a cloud of particles in a stratified environment is not well investigated. Noh (2000) studied settling of a cloud of particles through a 2-layered environment. He found a cloud of particles settles uniformly keeping its cloud shape if it is in the particle settling regime ($X = q/l{w_s}^2 \ll 1$), where l is the depth of the density interface; however, when the front of the cloud of particles hit the density interface, the cloud of particles spreads horizontally along the density interface forming a turbidity current—which is a fast-moving, sediment-laiden fluid—if it is in the thermal regime ($X \gg 1$). In the latter case, the turbidity current can last as long as its virtual density is

lighter than that of the bottom layer, but it disappears soon because the particles escape while propagating and accordingly the turbidity current loses its momentum.

Bush *et al.* (2003) studied a cloud of particles in a linearly stratified column. They found when the stratified cloud number, $N_s = w_s Q^{-1/4} N^{-1/2}$ (Luketina & Wilkinson 1994), is bigger than unity, the cloud initially sinks as a thermal, then particles in the cloud fall out as a bowl-shaped swarm at a certain depth and the rest of fluid associated in the cloud ascends to the depth which matches its density. A vertical oscillation of the remaining fluid was observed at a frequency close to N, the buoyancy frequency of the ambient stratification. When $N_s < 1$, the cloud initially sinks as a thermal; however, the whole cloud overshoots the neutral depth, bounces back, and intrudes at the depth of its neutral buoyancy forming a gravity current. The particles in the cloud fall out between the maximum penetration depth and the neutral depth in an irregular shape.

To the author's knowledge, no work has been done with clouds of porous spheres, the density of which is initially lower than that of the BL fluid but higher than that of the TL fluid. If the porous sphere is large enough that the diffusive uptake of salt from the ambient fluid takes for a certain period of time until it gains an excess negative buoyancy, the porous spheres in the cloud would be temporarily trapped at their neutral depth regardless of X or N_s. On the other hand, if the porous spheres are so small that the diffusive fluid exchange occurs instantly, the settling behavior of the porous sphere cloud may be similar to the case of the solid (or non-porous) particle settling.

Methods

Experimental scheme

Porous spheres

The spheres used in this study were made of agarose. Smaller spheres (diameter: 50–300 μm) were supplied from a commercial supplier (ABT), and larger spheres were made in the laboratory according to Kiørboe *et al.* (2002). Agarose solution was prepared by microwaving agarose powder (Sigma Aldrich) and deionized (DI) water in a flask. Then, it was dripped into a beaker containing cooler DI water with a 1.5–2 cm thick mineral oil layer on the top. A pipette was used to drip the agarose solution, and the end of the pipette tip was cut to widen its mouth. The size of manufactured spheres ranged from 0.8 to 3 mm (figure 1).

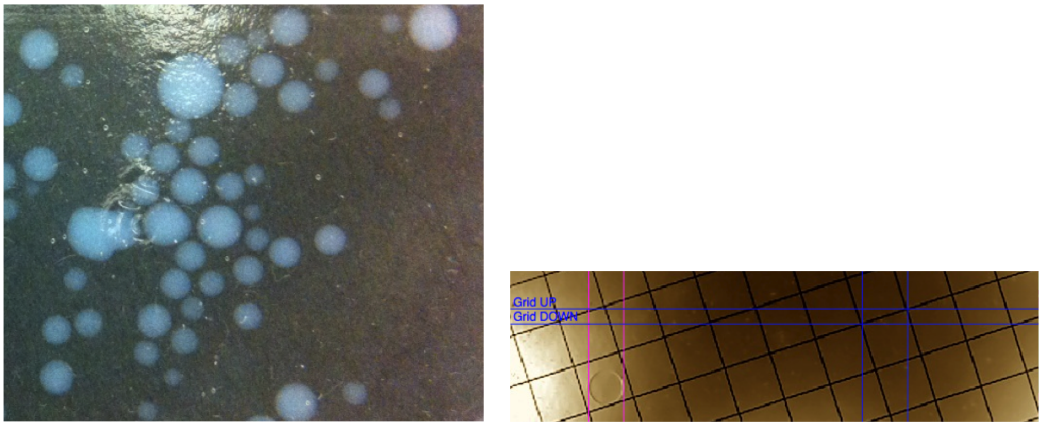

(*a*) (*b*)

Fig. 1: Manufactured agarose spheres (a) and the measurement of their sizes on a slide with 1 mm grid spacing (b).

Water column stratification

An acrylic water tank (28 cm L x 28 cm W x 60 cm H, inner dimension) was used to set up three kinds of water columns: 1) homogeneous water column, 2) sharp 2-layer stratified water column, and 3) linearly stratified water column. For a 2-layer stratification, BL fluid with a higher density was poured first, and TL fluid, which was always DI water, was introduced slowly using a diffuser, a sponge with a styrofoam rim which floats on water. For linear stratification, BL fluid was poured to a certain height, then Oster's (1965) two vessel technique was applied to make a linearly stratified region, and finally TL fluid was introduced at the top using the diffuser. For some experiments, a same 2-layered water column sit for an extended period of time to make its stratification thicker (figure 21 (c)).

After setting up a stratified water column, temperature and conductivity were profiled every 1 cm or 0.5 cm around the density interface from the bottom to the top using a sensor (MSCTI Model 125, PME Inc.), then converted to density using Gibbs-SeaWater (GSW) Oceanographic Toolbox (McDougall & Barker 2011). However, due to the discrepancy of the composition between the real seawater and a NaCl solution, GSW Oceanographic Toolbox does not return the actual density of the NaCl solution. Accordingly, it was scaled using the actual densities of BL and TL fluids, which were measured by a density meter (DMA 35, Anton Paar).

Video imaging

A monochrome camera (Pike F-100C, AVT) with computer imaging acquisition software (SmartView, AVT GmbH and StreamPix, NorPix Inc.) was used. An LED light panel was placed on each of two opposite side walls of the water tank during experiment, and images were

taken at about 8 or 16 frames per second (figure 2). The frame size was 1,000 x 1,000 pixels at maximum with bit depth of 8 or 16 bit/pixel. The timestamp function on the software did not return the right time information due to an unknown computer error, so time information was reconstructed using an average time interval (the total number of images / [the oretime the last image was taken - the time the first image was taken]).

Experiments

Single sphere experiment. Water columns with different stratification were made, then the water tank was covered with a specially designed lid to prevent effects from any free surface disturbance, which was submerged to a depth of about 2 cm. The lid had a 4 mm diameter hole at its center, where a sphere was released. Another hole, wider than the center hole, for a conductivity and temperature measuring probe was located at each of the four corners. After the diameter of a sphere was measured using a gridded slide with a digital microscope (26700-300, Aven Inc.), the sphere was taken gently by a pipette, and released to the water column through the center hole of the lid. Images were acquired while the sphere was settling. At the end of each experiment, an image of a ruler in the tank was captured to scale the pixel size. The spheres were collected to use in other experiments. All spheres were always hydrated in TL fluids before experiment.

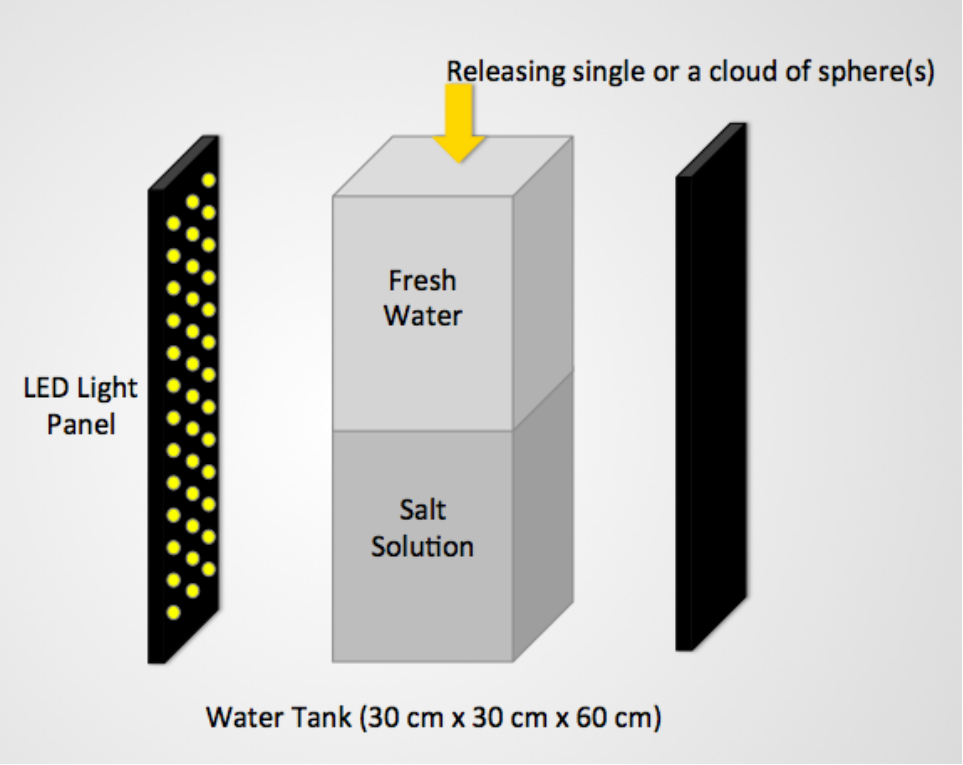

Fig. 2: Experimental setup. The water tank with inner dimensions of 28 cm L x 28 cm W x 60 cm H was built of acrylic. LED lighting apparatuses were placed on each side of the tank. The water column was homogeneous or stratified according to the purpose of the experiment. A single sphere or a cloud of spheres was released from the top of the tank. For single sphere releasing experiments, an acrylic lid with a center hole sat just below the water surface in order to eliminate disturbances due to the free surface.

Cloud of spheres experiment. Experimental procedures were identical to that of the single sphere experiment, except for the sphere preparation stage and the presence of a lid. The lid was not used, since the free surface disturbance was not as significant as in the case of the single sphere experiments. The spheres were sorted by using sieves with different mesh sizes (0.053, 0.100, 0.150, 0.180, 0.250, 0.300, 1.00, 1.40, 1.70, 2.00, 2.36, 2.80 mm, Cole-Parmer). Then, each was weighed on a balance and made into a cloud solution with a certain concentration of spheres (known weight of spheres to a total weight of the spheres and DI water). Large-sphere clouds, with the total weight of 9.2 or 10 g, were released using a stemless funnel and a plunger as decribed in Bush *et al.* (2003). However, clouds of small spheres, with total volume of 1 cm^3, was released by a pipette slowly. The concentration of spheres in a cloud was always 25% (25% of spheres and 75% of DI water by weight).

Image processing

Preconditioning. Images were processed using MATLAB (MathWorks) and DataTank (Visual Data Tools Inc.). First, the size of an image was cropped to exclude the non-working area, and

the background image, which was usually set to be the image at $t = 0$, was subtracted from the cropped image. Then, low-value signals under a threshold (1–2 % of the saturated value of a pixel) were removed from all pixels in each image.

Single sphere tracking. The initial location of a sphere at $t = 0$ was picked manually, and then the sphere was tracked automatically with the following algorithm: 1) set a small region around the sphere, 2) identify all dots in the region, 3) pick dots bigger than a certain area, which is a number of connected pixels, 4) find a dot with the largest area, which is assumed to be the sphere, and 5) if the number of dots with the largest area are more than two, find a dot which is the closest to the previous sphere position. The centroid of the connected pixels in a dot was set as a position of the sphere. Finally, the trajectory was smoothed using a Butterworth filter in order to remove fluctuations due to a fairly large pixel size that is comparable to the size of the sphere.

Cloud of spheres tracking. The centroid of the whole cloud was tracked for each image using the following equation,

$$Z_c(t) = \int_0^{z_n} \left(z \frac{\int_0^{x_n} i(x,z,t)dx}{\int_0^{x_n}\int_0^{z_n} i(x,z,t)dzdx} \right) dz \tag{7}$$

where Z_c is the vertical location of centroid, z_n is the vertical length of the image in pixels, x_n is the horizontal length of the image in pixels, and $i(x, z, t)$ is the signal intensity at (x, z) at time t. Also, 2nd, 3rd, and 4th moments were calculated to investigate the shape of a cloud:

$$Standard\ deviation,\ SD(t) = \sqrt{\int_0^{z_n} \left((z - Z_c(t))^2 \frac{\int_0^{x_n} i(x,z,t)dx}{\int_0^{x_n}\int_0^{z_n} i(x,z,t)dzdx} \right) dz}, \tag{8}$$

$$Skewness(t) = \frac{1}{SD(t)^3} \int_0^{z_n} \left((z - Z_c(t))^3 \frac{\int_0^{x_n} i(x,z,t)dx}{\int_0^{x_n}\int_0^{z_n} i(x,z,t)dzdx} \right) dz, \tag{9}$$

$$Kurtosis(t) = \frac{1}{SD(t)^4} \int_0^{z_n} \left((z - Z_c(t))^4 \frac{\int_0^{x_n} i(x,z,t)dx}{\int_0^{x_n}\int_0^{z_n} i(x,z,t)dzdx} \right) dz. \tag{10}$$

Numerical models

Sinlge sphere model

The model calculates the location of a porous sphere at each time step (schematic diagram of the model is shown in figure 3). Letting the center of ambient stratification be at $z = 0$ and z increases toward the direction of gravity, the settling velocity of the sphere is

$$U(t) = \frac{dz_p}{dt}$$

where z_p is the position of the sphere. Then, it is discretized with a forward time scheme,

$$z_{p_{t+1}} = z_{p_t} + \Delta t \cdot U_t.$$

$\frac{dU}{dt}$ was discretized from equation (2) with forward time scheme,

$$U_{t+1} = U_t + \Delta t \left(-\frac{3\rho_f C_D U^2}{8\rho_s a} + \frac{\rho_s - \rho_f}{\rho_s} g \right)$$

where a is the radius of a sphere. The initial velocity, U_0, is an arbitrarily assigned small number since C_D cannot be defined when $U = 0$.

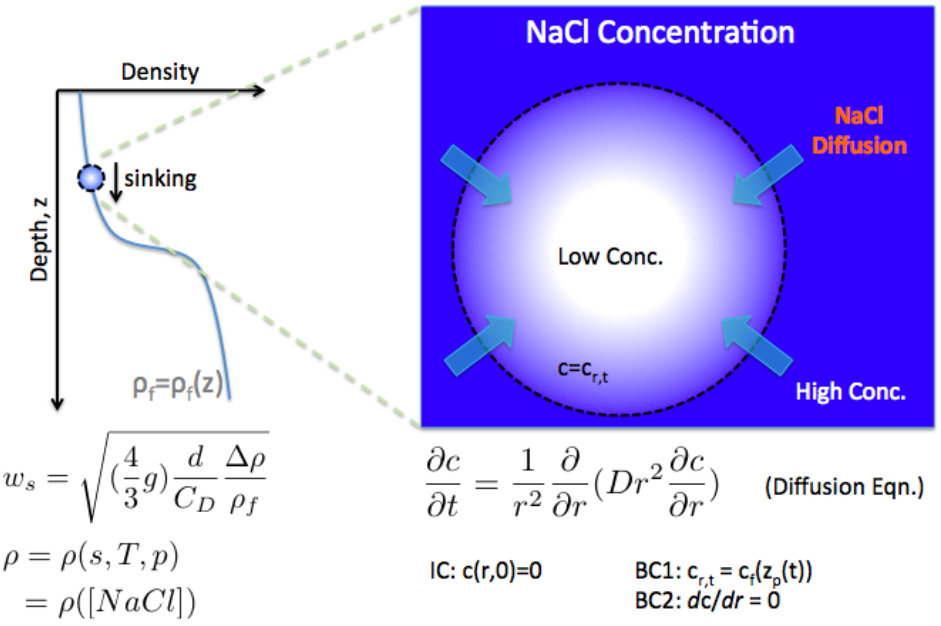

Fig. 3: Schematic diagram of the numerical model. The left shows a density profile of a stratified water column. When a porous sphere settles in a stratified water column, it experiences a change in $\Delta\rho$, the density difference between the sphere and the ambient fluid. $\Delta\rho$ is a key control factor of settling speed. Because all experiments were performed at room temperature and the water column height was only 60 cm, density of fluid becomes a function of the concentration of salt (NaCl) in this study. As the sphere was porous, salt molecules are diffused from the ambient fluid to into the sphere since the settling sphere has lighter interstitial fluid than the ambient fluid at depth. The diffusion equation was adapted to our model with an initial condition that the salt concentration ([NaCl]) is initially zero and two boundary conditions: 1) [NaCl] of the interstitial fluid on the sphere's surface is identical to that of the surrounding ambient fluid and 2) the gradient of [NaCl] at the center of sphere is zero.

In the presence of ambient stratification, a porous particle changes its density until equilibrium as long as the density of interstitial fluid of a sphere ($\rho_{f'}$) is different than that of ambient fluid (ρ_f). Diffusion equation (equation (5)) was discretized with forward time and central space schemes,

$$C_{r,t+1} = C_{r,t} + \Delta t[k_1 C_{r+1,t} + k_2 C_{r,t} + k_3 C_{r-1,t}],$$

$$k_1 = \frac{D}{r\Delta r} + \frac{D}{\Delta r^2}, \qquad k_2 = -\frac{2D}{\Delta r^2}, \qquad k_3 = -\frac{D}{r\Delta r} + \frac{D}{\Delta r^2},$$

where $C_{r,t}$ is a concentration of salt at a point with a distance of r from center and at time of t, Δr is a spatial grid spacing, and Δt is a time step spacing. The initial salt concentration of the interstitial fluid was assumed to be zero. For each time step, the boundary conditions change. To calculate the $C_{r,t+1}$, $C_{0,t}$ and $C_{a,t}$ were substituted with $C_{dr,t}$ and $C_f(z_p(t))$, respectively.

The average concentration of salt of the interstitial fluid, C_{avg}, was calculated using equation (6),

$$C_{avg}(t) = \sum_{i=0}^{nr-2} \frac{4}{3}\pi[(dr \cdot (i+1))^3 - (dr \cdot i)^3] \frac{C_{dr\cdot(i+1),t} - C_{dr\cdot i,t}}{2}$$

where nr is the number of spatial grid points along the radial axis, and dr is the spatial grid spacing. Then, C_{avg} was converted to $\rho_{f'}$. Then, ρ_s was calculated using equation (4).

White's (1974) empirical drag law (equation (3)) was used for C_D. The ambient density profile ρ_f was approximated to a fitted curve from each experiment. An error function fit was used for 2-layered stratification,

$$\rho_f(z/\sqrt{4Dt^*}) = \overline{\rho_f} + \frac{\Delta\rho_f}{2} erf(z/\sqrt{4Dt^*})$$

where t^* is the characteristic time which best fits the measured density profile. Also, a piecewise cubic Hermite interpolating polynomial function fit was used for linear stratification.

Cloud model

Assuming no interparticle effects, a cloud of spheres was modeled as a histogram of the vertical positions of n single spheres with different sizes. Also, all particles were assumed to be at rest at $t = 0$, and accordingly, the model did not demonstrate a thermal phase which occurred upon the release of a cloud of spheres in experiment. First, the single sphere model described above was simulated to obtain the vertical location, z_p, at each time for spheres with the range of sizes ($z_{a_1}, z_{a_2}, z_{a_3}, \cdots, z_{a_n}$ where a_n is the radius of sphere and $a_n - a_{n-1} = constant$). Then, assuming the size distribution of spheres in the cloud is a normal distribution, each sphere was weighted according to its size frequency by multiplying by its probability density function, $p = p(a)$. This was again multiplied by an arbitrary intensity function ($I(a) \propto a^3$), a function of the scattered light intensity according to sphere size, to demonstrate the actual experimental condition. At each time step, all spheres' locations were binned to a gridded vertical axis. In this manner, the vertical distribution of spheres was tracked at each time point.

Results

Three main sets of laboratory experiment were conducted to investigate the settling behavior of porous spheres in the present of stratification: 1) settling of single spheres in homogeneous water columns, 2) settling of single spheres in stratified water columns, and 3) settling of sphere clouds in stratified water column. Porous spheres made of agarose were used as a proxy for marine snow, and sodium chloride was used as a stratifying agent. By using these laboratory-manufactured spheres, the potential uncertainties caused by the irregular shape, porosity, and solid matrix density of real marine snow could be excluded while maintaining key parameters (e.g. porosity and stratification type). The parameters utilized in the experiments were sphere size, type of density stratification, and porosity (table 2). In addition, numerical simulation was conducted to demonstrate both settling of a single sphere and of a cloud of spheres. Then, results from the lab experiments were compared with that from the numerical simulation.

ID	Radius (mm)	ρ_{TL} (g/cm^3)	ρ_{BL} (g/cm^3)
Homogeneous Column			
1†	table 3	0.9982	—
2†		1.0108	—
3†		1.0216	—
4†		1.0300	—
5†		1.0407	—
2-Layer Column			
6	table 3	0.9987	1.0214
7		0.9982	1.0413
Linear Column			
8	table 3	0.9982	1.0216
9		0.9986	1.0407

(a) Single sphere experiment list. (†: the experiment were repeated three times.)

ID	Diameter (mm)	Releasing Amount	Sphere Concentration (%)	ρ_{TL} (g/cm^3)	ρ_{BL} (g/cm^3)
2-Layer Column					
10	1.00–1.40, 1.40–1.70, 1.70–2.00	10 g	25% spheres + 75% TL fluid	0.9979	1.0225
11	2.00–2.36, 2.36–2.80	10 g		0.998	1.02
12‡	0.150–0.106, 1.40–1.70	$1ml$, 9.2g		0.9983	1.0220
13	0.053–0.106, 0.106–0.150 0.180–0.250, 0.250–0.300	$1ml$		0.9980	1.040
14		$1ml$		0.9980	1.0201
15		$1ml$		0.9980	1.0101

(b) Cloud experiment list. (‡: the experiment was conducted with five different density interface thicknesses.)

Table 2: List of experiments.

Homogeneous column experiment

The eight agarose (1%) spheres in table 3 were released in five different homogeneous water columns—0.9981, 1.0102, 1.0216, 1.0300, and 1.0406 g/cm^3. For each column, three sets of

repetitive experiments were done.

Sphere ID	1	2	3	4	5	6	7	8
Radius (mm)	0.4266	0.4451	0.5380	0.6260	0.6576	0.7826	0.8512	0.9413
Re in Fresh Water	1.3246	1.5287	2.3631	3.4739	3.8325	5.6344	6.9021	8.5932

Table 3: Agarose spheres used for a single sphere experiment. The ID, radius, and Reynolds number of each sphere are shown in the first, second, and third rows, respectively.

The vertical position of a sphere was plotted for the entire time domain. However, in some cases, fluctuation existed near the bottom. Accordingly, the top 50 pixels and the bottom 300 pixels were cropped (figure 4). The trajectories in the cropped region were each fit with a line by the least squares method, and the slope of each curve was the terminal settling velocity, w_s. As each experiment was repeated three times, the mean value of the three became the final settling velocity used for further analysis.

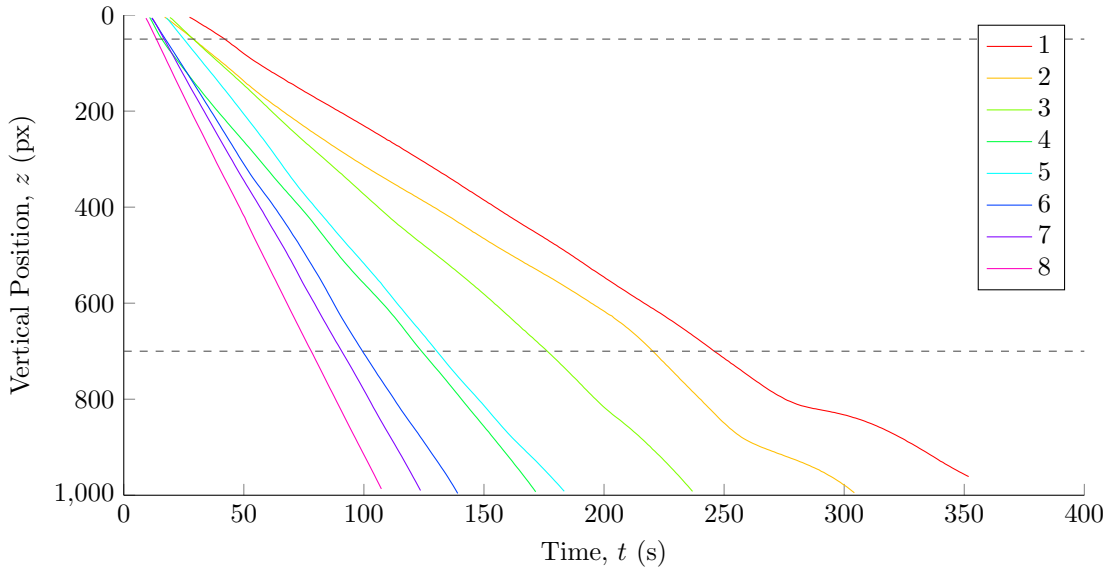

Fig. 4: Vertical trajectories of the eight agarose spheres (table 3) in a homogeneous column with 1.0406 g/cm^3. Each different color marks a different sphere whose ID number is shown in the box at the top right corner. Only the middle section between the two dashed lines was used to calculate the settling velocity of each sphere.

Equation (2) with $dU/dt = 0$ and $U = w_s$ is rearranged to

$$\rho_s = (\frac{3C_D {w_s}^2}{4dg} + 1)\rho_f.$$

The total density of each sphere was calculated with the above equation using w_s from experiment.

Then, the porosity, P, and the solid matrix density, ρ_m, were calculated by linear regression

between ρ'_f and ρ_s using equation (4). As the spheres were hydrated in the same fluid of the water column before experiment, ρ'_f was identical to ρ_f. The porosity was 0.9916 and the matrix density was 1.5215 g/cm^3 (figure 4). These values were used for the numerical model simulation.

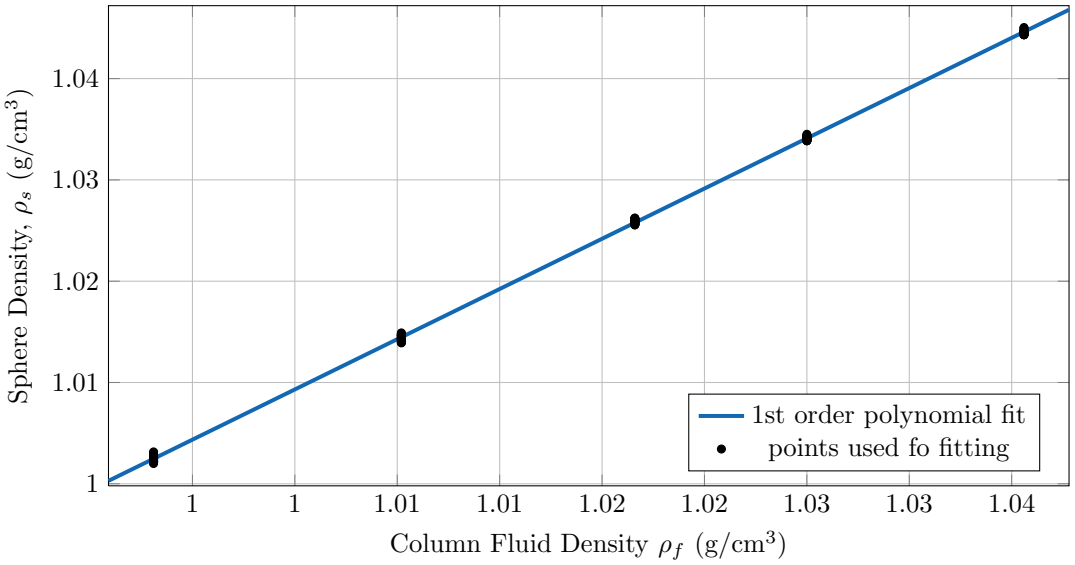

Fig. 5: Linear regression between the water column density and the sphere density. According to equation (4), the slope of the linear regression line is the porosity (P) of agarose spheres, and the y-intersect is the product of $(1 - P)$ and the density of matrix, ρ_m. $P = 0.9916$ with 95% confidence interval $[0.9886, 0.9947]$, $\rho_m = 1.5215$ with 95% confidence interval $[0.8624, 2.1806]$, $R^2 = 0.9997$.

2-Layer stratification experiment

In the presence of stratification, regardless of its type and the strength (figure 6), all spheres show delayed settling around and inside the stratification (figure 7). A larger sphere reaches the entrance of the stratified region earlier but escapes later than a smaller one (e.g. compare the results of sphere 1 and 8 in figure 7). Also, we can observe the sphere's speed gain when it escapes the stratification region is slower than its speed loss when it enters the region (e.g. compare the first and second kinks of each line in figure 7). This is because the sphere needs only a slight negative buoyancy to escape the stratification and to settle through BL water.

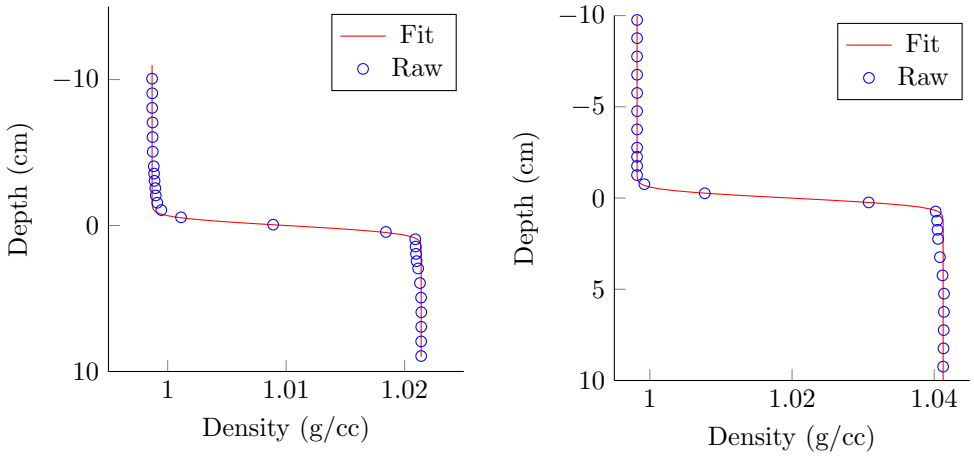

(a) 2 Layer (BL 1.0216 g/cc)

(b) 2 Layer (BL 1.0406 g/cc)

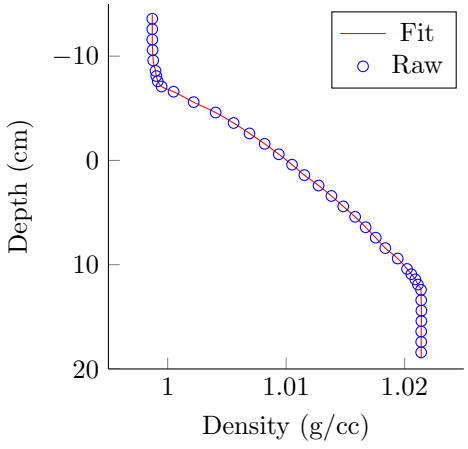

(c) Linear (BL 1.0216 g/cc)

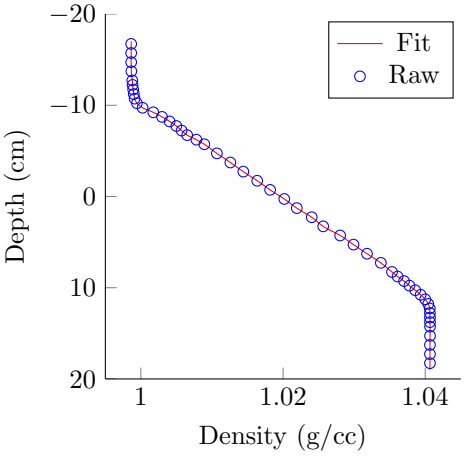

(d) Linear (BL 1.0406 g/cc)

Fig. 6: Density profiles of water columns used for a single sphere settling experiment. The blue circles are the measured densities using a CT probe, and the red lines are the fitted curves—an error function was used for a and b, and a piecewise cubic Hermite interpolating polynomial function was used for c and d. ρ_{top} was always fresh water, while ρ_{bottom} was 1.0216 g/cm^3 (a and c) and 1.0406 g/cm^3 (b and d). Experiments were done in both sharp 2-layered stratification (a and b) and linear stratification (c and d).

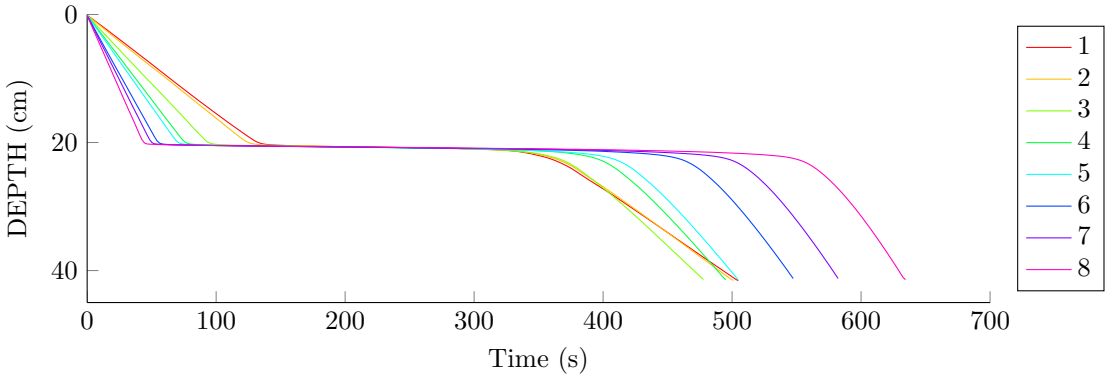

(a) 2 Layer (BL 1.0216 g/cc)

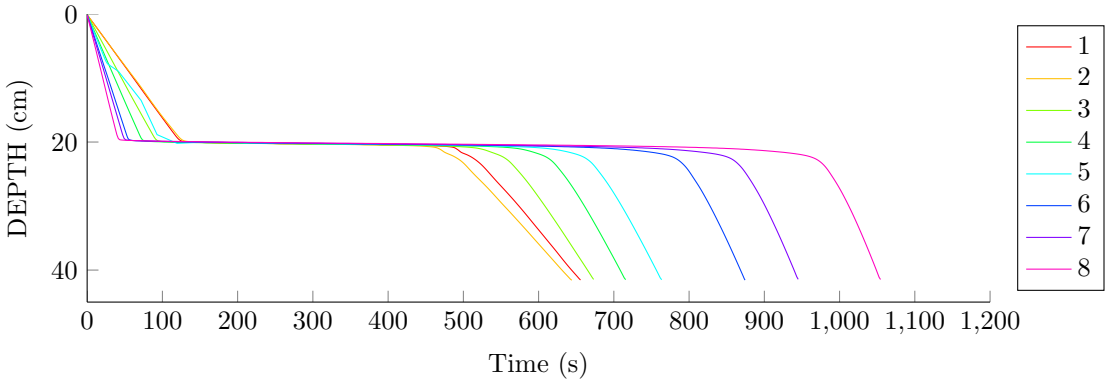

(b) 2 Layer (BL 1.0406 g/cc)

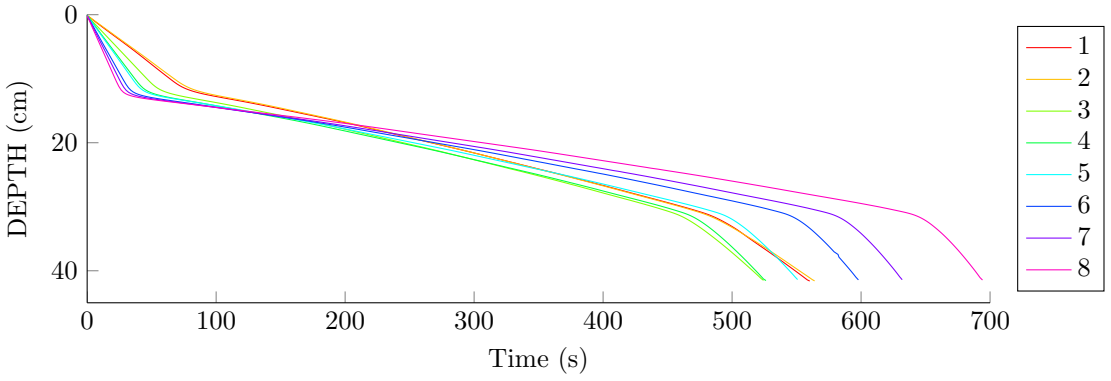

(c) Linear (BL 1.0216 g/cc)

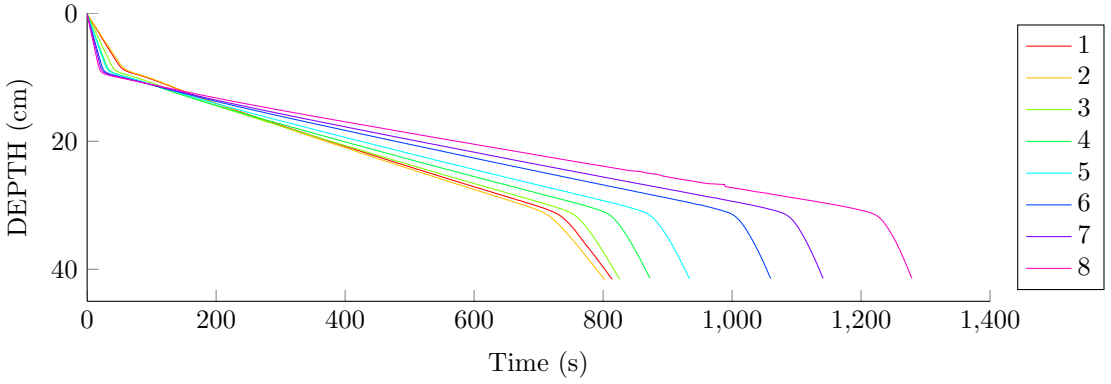

(d) Linear (BL 1.0406 g/cc)

Fig. 7: Vertical trajectories of the eight agarose spheres (in table 3). The first two figures (a and b) are in the sharp 2-layer stratification (as in figure 6 (a) and (b)), and the last two figures (c and d) are in the linear stratification (as in figure 6 (c) and (d)).

The single most important parameter is a time scale of delayed settling due to stratification, because it has important ecological implications—e.g. the amount of POC remineralized or consumed by microbes and zooplankton is related to the time that POC spends in the water column. To measure the time scale, residence time, τ_r, was introduced (figure 8). τ_r was defined as the time taken to settle through a stratified region. The stratified region was defined as the region where the local density gradient is equal to or greater than one thousandth the maximum local density gradient (z where $\frac{d\rho_f}{dz} \geq 0.001 max(\frac{d\rho_f}{dz})$, figure 8 (c)). In addition, residence time normalized by settling time scale, τ_r/τ_s, was used when necessary. The settling time scale, τ_s was defined as

$$\tau_s = \frac{1}{2}(\frac{l_{box}}{w_{TL}} + \frac{l_{box}}{w_{BL}}) \tag{11}$$

where l_{box} is the vertical length of the stratified region as defined in figure 8 (b), and w_{TL} and w_{BL} are the terminal settling velocities of the sphere in TL and BL fluids, respectively.

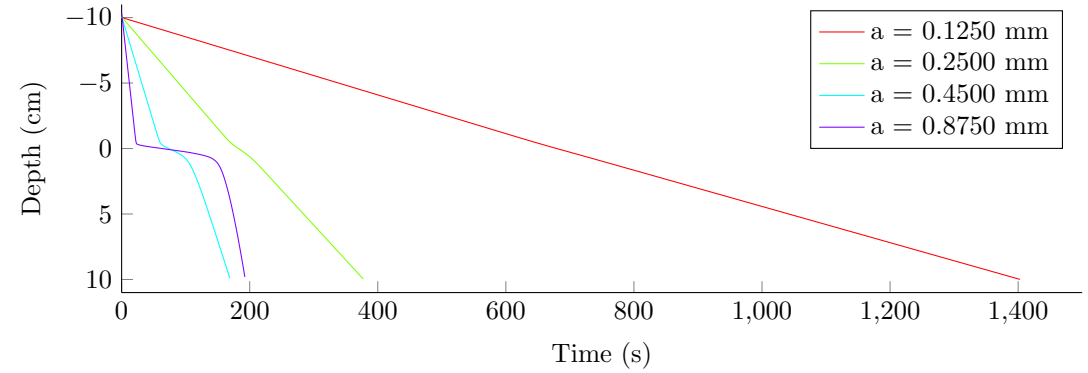

(a) Trajectories of single sphere

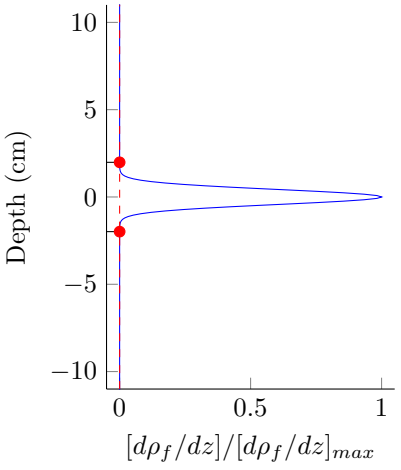

(b) The Definition of Stratified Region

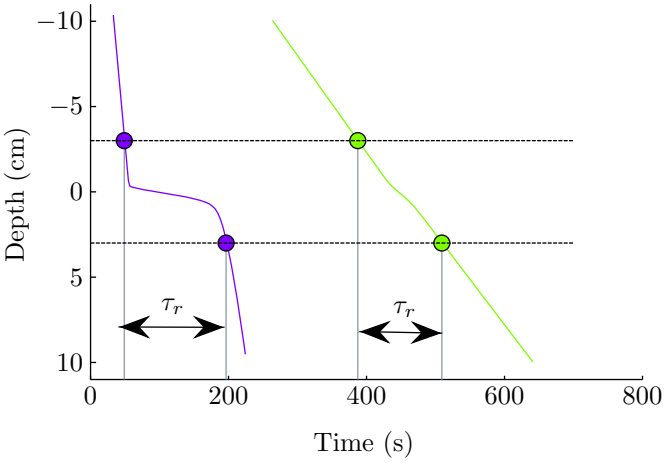

(c) Residence Time

Fig. 8: The definition of residence time, τ_r. The vertical position of a sphere over time (from the numerical simulation using profile of figure 6 (a), where the center of stratification is located at the zero depth) is shown in (a). The vertical length of the density region is defined as the region where $d\rho_f/dz$ is equal to or higher than 0.1% of the maximum $d\rho_f/dz$ (b). The residence time is the difference in two time points when a sphere passes the upper boundary and the lower boundary of the density interface (c).

The result shows a trend that a larger sphere has a longer τ_r in both 2-layered and linear stratifications (figure 9). A larger sphere had a larger interstitial volume initially containing TL fluid, which was always fresh water. Accordingly, compared to a smaller sphere, a larger sphere takes a longer time to exchange the lighter interstitial fluid with the denser ambient fluid. Also, it is observed that a stronger density stratification delays the settling of a sphere longer than a weaker one, because a sphere should take more salt by molecular diffusion to be denser than BL fluid. The τ_r in a linear stratification is longer than that in a 2-layer stratification (figure 10), although in a linear stratification the settling speed of a sphere does not approach zero. This would be because linear stratification has a longer vertical length scale of stratification for a given $\Delta\rho_f$ than a 2-layer stratification. Therefore, settling through a longer length in linear stratification takes more time, while the time scale for diffusive process would be similar.

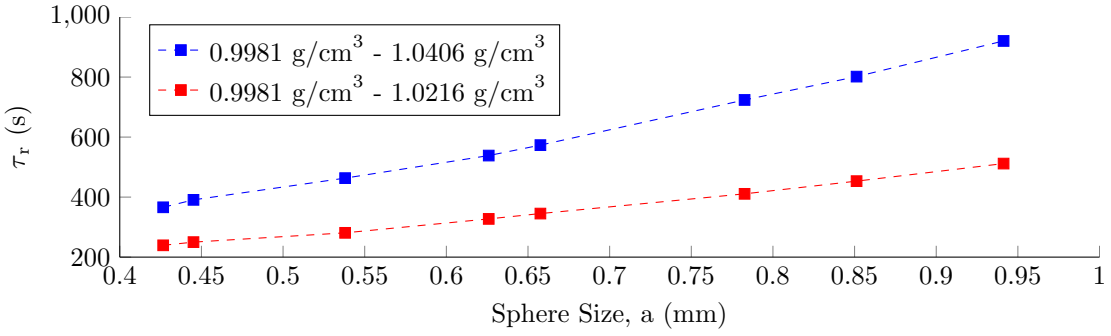

(a) 2 Layer

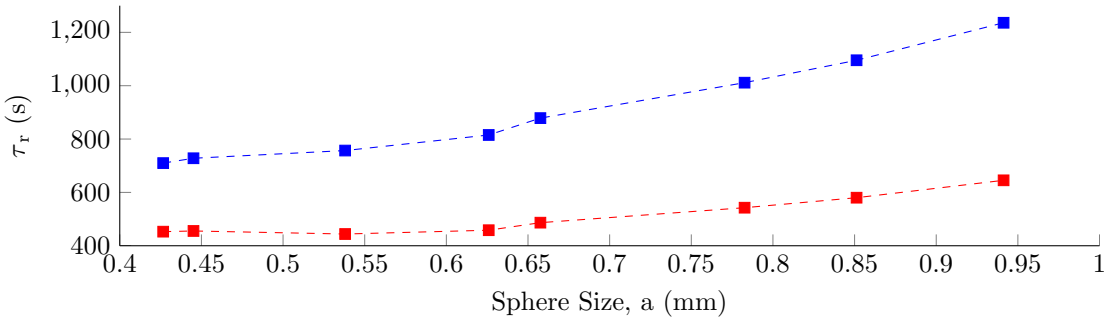

(b) Linear

Fig. 9: τ_r of a settling single sphere from experiments in 2-layer stratification (a) and in linear stratification (b). The density difference between top and bottom layers ($\Delta\rho_f$) was ~ 0.04 g/cm^3 (blue) and ~ 0.02 g/cm^3 (red). The spheres in table 3 were used.

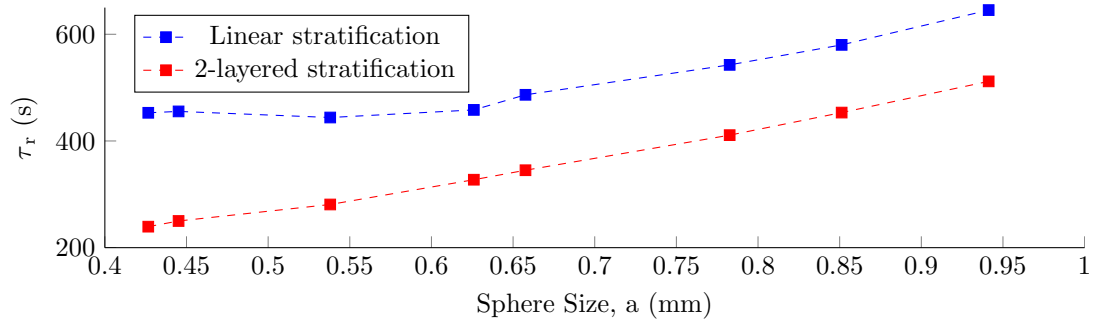

(a) (BL 1.0216 g/cc)

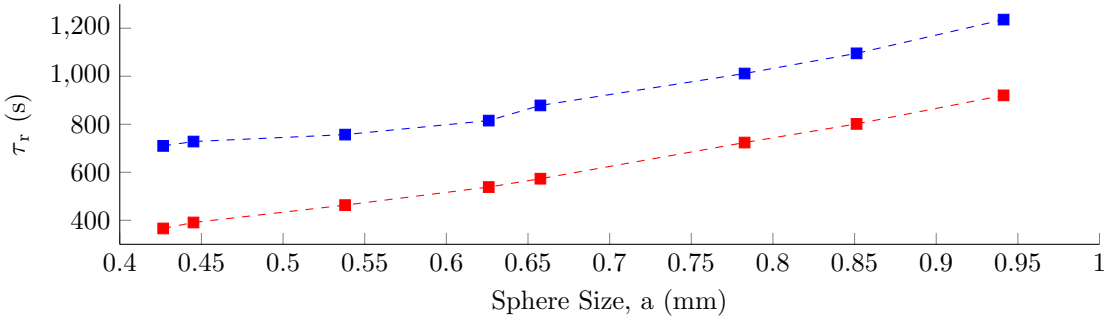

(b) (BL 1.0406 g/cc)

Fig. 10: τ_r of a settling single sphere from experiments in $\Delta\rho_f \cong 0.02$ (a), $\Delta\rho_f \cong 0.04$ (b). Water column stratification was linear (blue) and 2-layered (red). This figure and figure 9 share same data, but organized differently. The spheres in table 3 were used.

As shown in figure 11, the numerical model did not reproduce the experimental result per-

fectly. However, it seems to predict the tendency well, although the τ_r was significantly lower in the numerical simulation result than the experimental result (figure 13). The main reason is likely to be the entrainment of the buoyant TL fluid (Srdic-Mitrovic *et al.* 1999; Abaid *et al.* 2004; Camassa *et al.* 2009, 2010). The entrained fluid from the TL forms a shell of lighter fluid (figure 12) around a sphere, which acts as a barrier to molecular diffusion. Because the [NaCl] of the entrained fluid is lower than that of the ambient fluid, it slows down the diffusive exchange process.

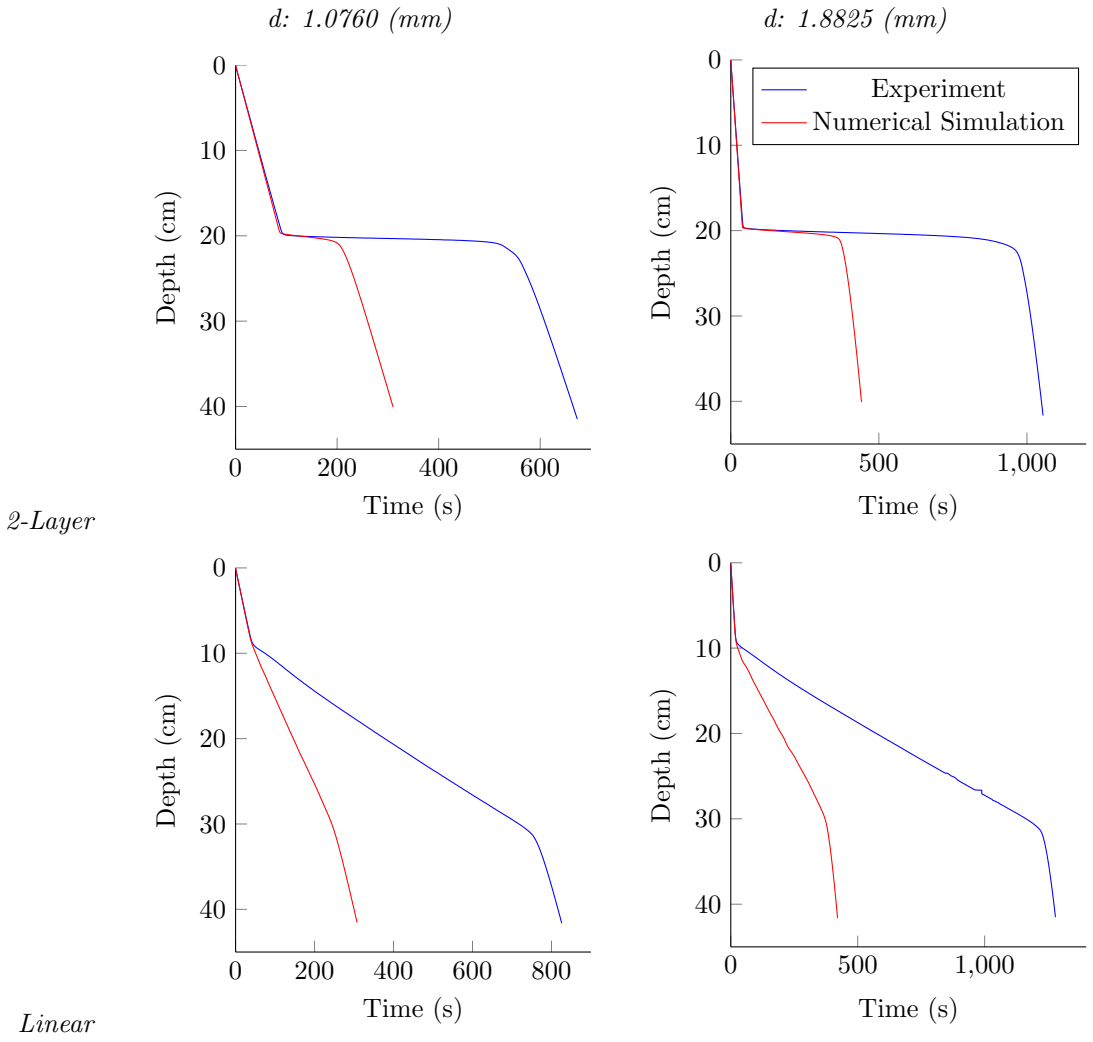

Fig. 11: Comparison of vertical trajectories between experimental (blue) and numerical (red) results in 2-layer stratification (top) and linear stratification (bottom) with $\Delta\rho_f \cong 0.04 g/cm^3$. Left figures are the result of the agarose sphere with 1.0760 mm diameter, and right figures are the result of the agarose sphere with 1.8825 mm diameter.

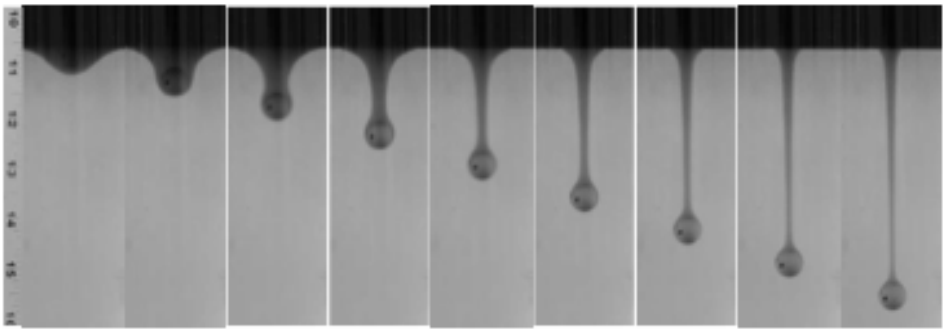

Fig. 12: Entrainment of fluid (adapted from Camassa *et al.* 2009). A sphere with 0.635 cm radius and a density heavier than BL fluid was released from the top in a stratified fluid column in a acrylic cylinder with 9.45 cm radius. The pictures were taken every 10 seconds. The TL fluid was the mixture of pure corn syrup and dye with the density of 1.37661 g/cm^3, while the BL fluid was the mixture of pure corn syrup and salt with the density of 1.38384 g/cm^3.

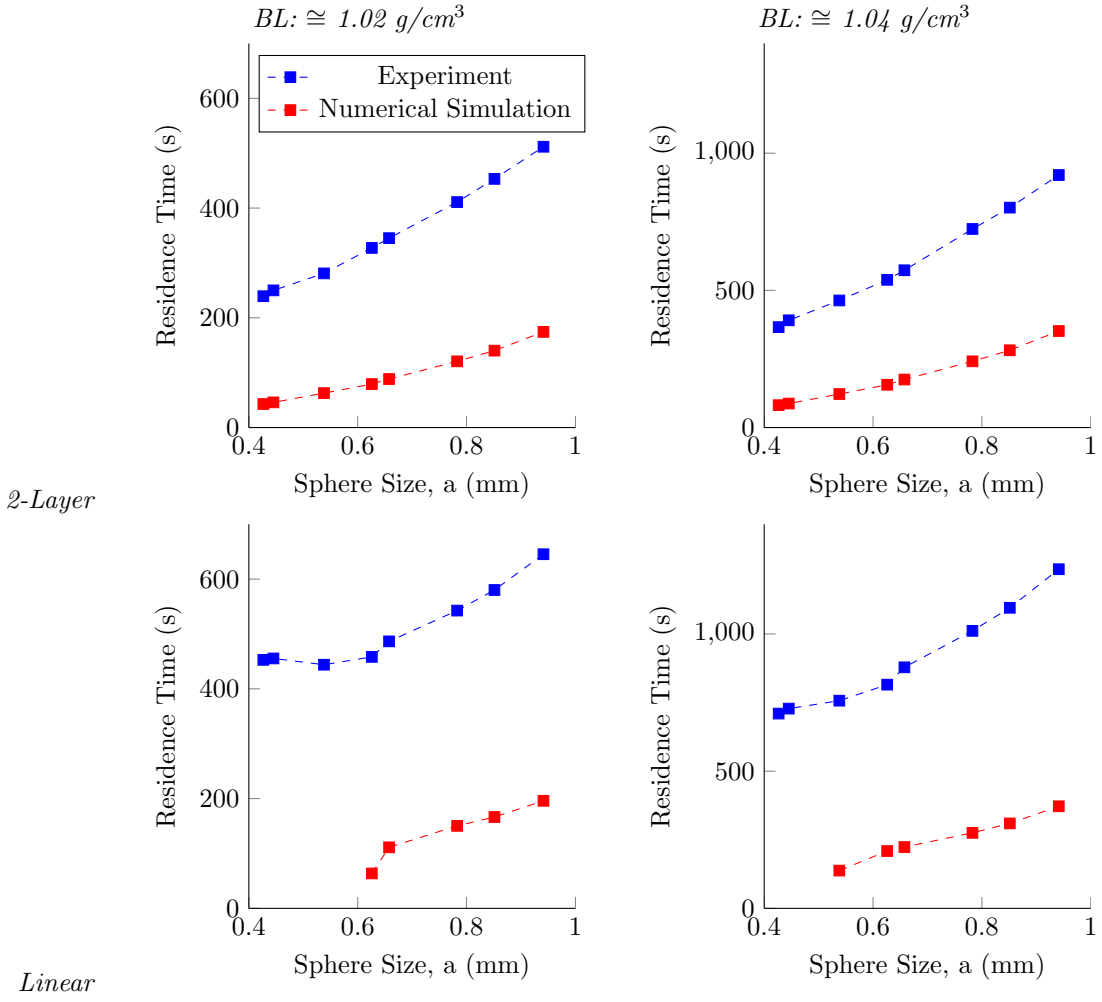

Fig. 13: Comparison of τ_r between experimental (blue) and numerical (red) results in 2-layer stratification (top) and linear stratification (bottom). The density difference between top and bottom layers ($\Delta\rho_f$) is ~ 0.02 g/cm^3 (left) and ~ 0.04 g/cm^3 (right). The spheres in table 3 were used.

The settling behavior of smaller spheres (< 0.4 mm radius) was investigated only through numerical model simulation because of the limitation of experimental technique. Imaging such a

small particle was not implementable with the current experimental setup. In addition, porous spheres in this size range could not be manufactured with the same method in the laboratory. When a sphere is smaller than a certain size, τ_r decreases with the size of the sphere (figure 14 (a) and (c)). On the other hand, the opposite is true for a sphere that is larger than a certain size. When a porous sphere is smaller than a certain size, it seems that a diffusive process is less important for a smaller sphere than a larger sphere that because equilibration occurs relatively faster due to a lesser volume of interstitial fluid. In such a case, physical settling rates would be more important. A smaller sphere has a smaller settling velocity, and accorindingly, it has a longer time to settle through the stratified region. This can be also seen using τ_r/τ_s (figure 14 (b) and (d))—for smaller spheres, τ_r/τ_s is ~ 1.

It seems that two main regimes exist for settling of a single porous sphere through stratification. When a porous sphere is smaller than a certain size, settling process is governed by settling process (settling regime). On the other hand, when a porous sphere is larger than a certain size, settling process is governed by diffusion process (diffusion regime). The transition size range between the two regimes might be around the size, with which a sphere has the lowest τ_r.

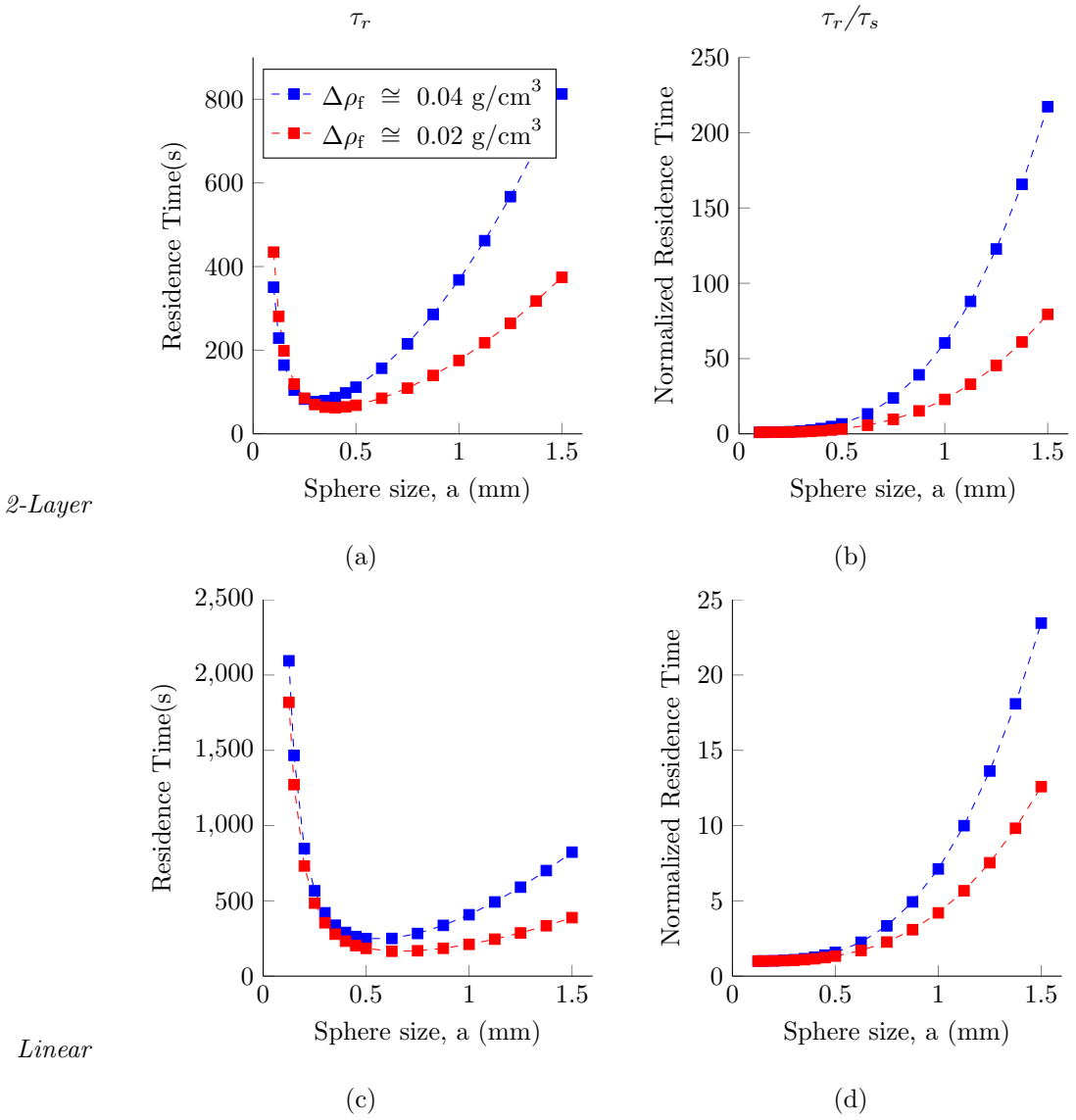

Fig. 14: τ_r and τ_r/τ_s from the numerical simulation. The water column density profile of experiment #6–9 in table 2 was used (figure 6). The vertical lengths of density interface region was 3.09 (blue) and 3.97 (red) cm for 2-layer stratifications (top) and 26.00 (blue) and 29.00 (red) cm for linear stratifications (bottom).

Settling of a cloud of porous spheres

Centroids were used to track the position of clouds for both experiment and numerical simulation, using equation (7). In general, the settling of a porous sphere cloud showed a similar behavior to that of an individual porous sphere. A cloud with larger spheres (a large-sphere cloud) nearly stopped settling in the stratified region (figure 15 (d) and (e)), while a cloud with smaller spheres (a small-sphere cloud) sharply decelerated its settling rate, but not stopped, in the stratified region (figure 15 (a), (b), and (c)). Accordingly, τ_r of clouds of spheres would also have a v-shaped trend similar to the settling of an individual sphere (figure 14)—τ_r of a cloud with spheres smaller than a certain size decreases with the sphere size (settling regime), while

that with spheres larger than a certain size increases with the sphere size (diffusion regime)—(figure 16, figure 17, and figure 18). This can be also inferred from τ_r/τ_s (figure 19). For small-sphere clouds, τ_r/τ_s is ~ 1, which indicates that τ_r is governed by settling process. On the other hand, for large-sphere clouds, τ_r/τ_s is an order(s) of magnitude larger than 1 and increases with the sphere size range of a sphere cloud. It indicates that τ_r of large-sphere clouds is not governed by settling process but involves other processes, among which molecular diffusion seems most important.

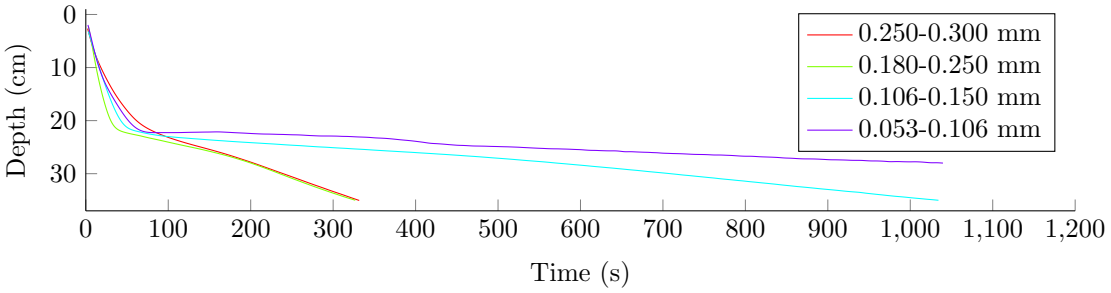

(a) Small-sphere cloud in 2-layer stratification ($\Delta\rho \cong 0.01 g/cm^3$).

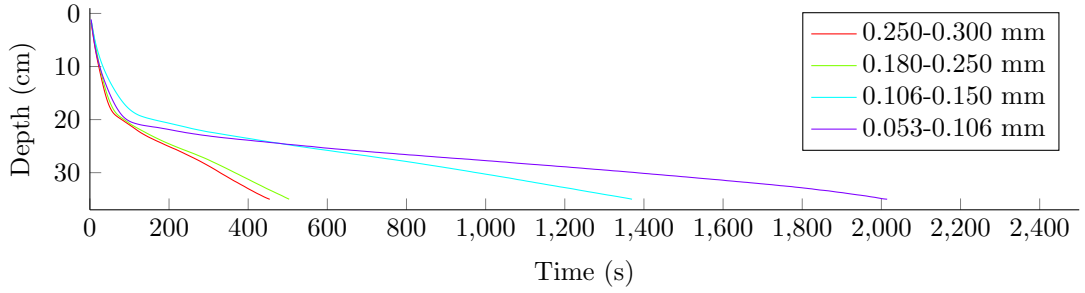

(b) Small-sphere cloud in 2-layer stratification ($\Delta\rho \cong 0.02 g/cm^3$).

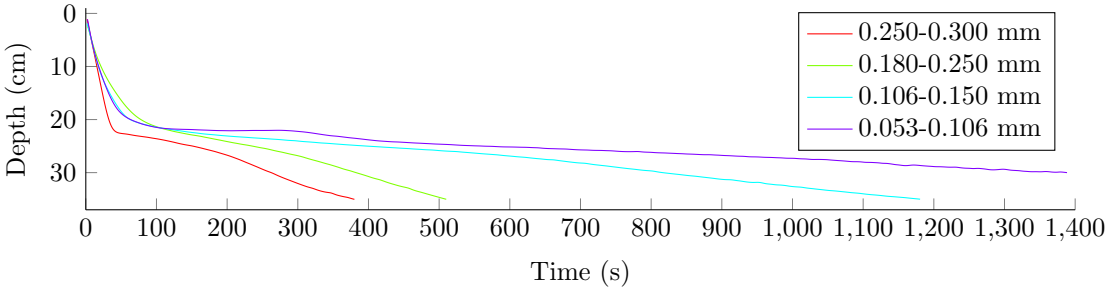

(c) Small-sphere cloud in 2-layer stratification ($\Delta\rho \cong 0.04 g/cm^3$).

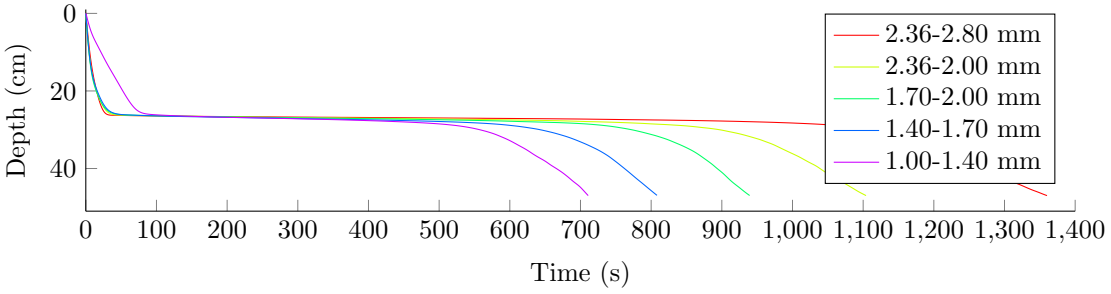

(d) Largel-sphere cloud in 2-layer stratification ($\Delta\rho \cong 0.02 g/cm^3$).

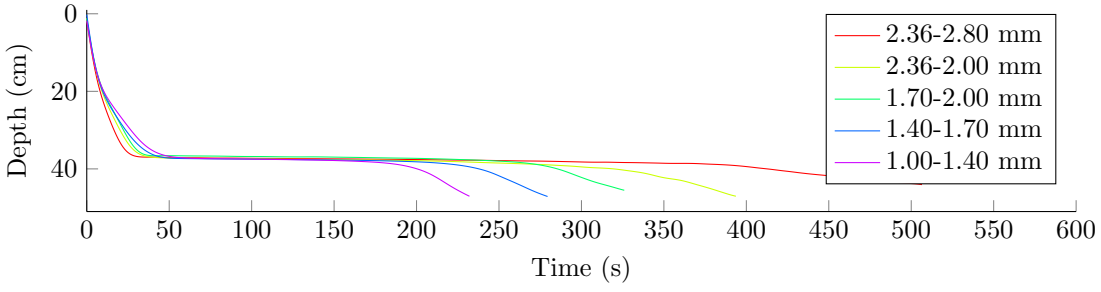

(e) Largel-sphere cloud in 2-layer stratification ($\Delta\rho \cong 0.02 g/cm^3$).

Fig. 15: Cloud centroid vs. time. $\Delta\rho_f$ was $\sim 0.02 g/cm^3$ in both experiments. The total releasing amount was 1 cm^3 (a, b, and c) and 8–10 g (d and e), while the sphere concentration was same in all experiments (25% w/w). The spheres were made of 4% agarose (a, b, and c), 1% agarose (d), and 2% agarose (e). All graphs were smoothed using the Butterworth filter.

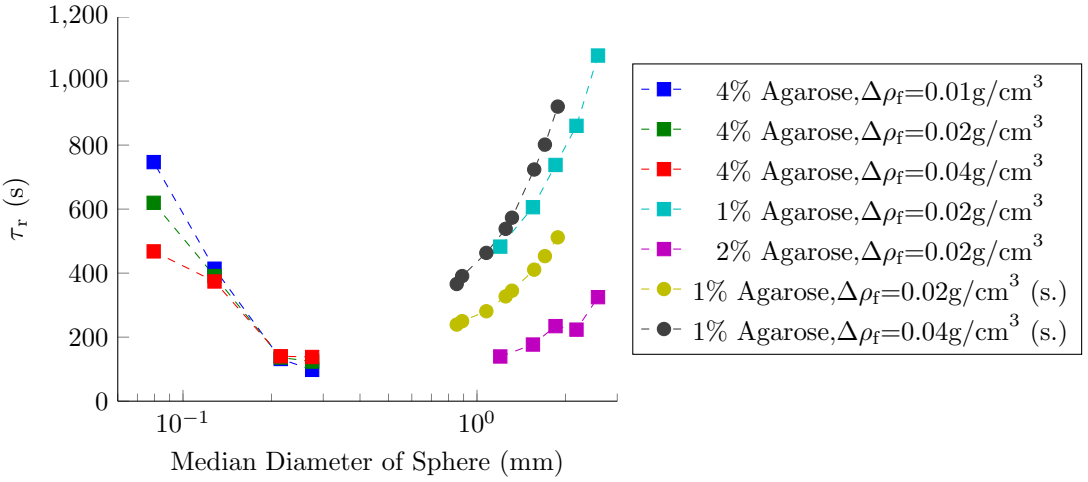

Fig. 16: τ_r of different clouds of spheres. τ_r of single sphere experiment are also plotted for comparison (yellow and dark grey). More details are in figure 17 and figure 18.

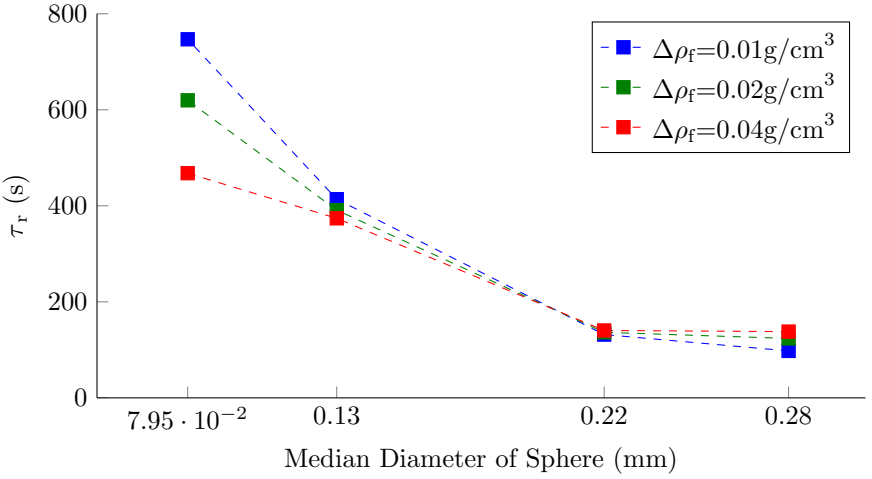

Fig. 17: τ_r of clouds of small spheres (53–300 μm) in different $\Delta\rho_f$. The total volume of each cloud was 1 cm^3 (25% of spheres and 75% of TL fluid (w/w)). The size range of each cloud was 53–106, 106–150, 180–250, 250–300 μm in diameter. Different colors show different $\Delta\rho_f$. The concentration of agarose of spheres was 4% in all experiments.

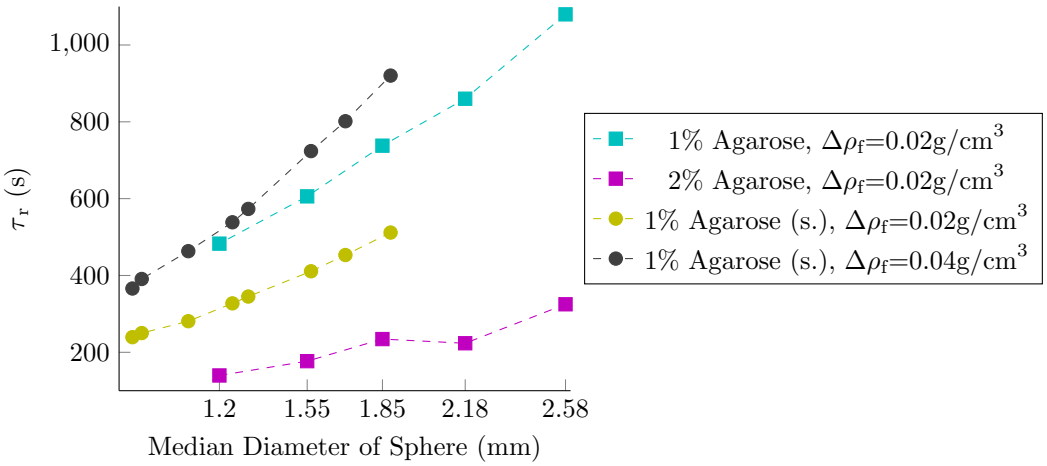

Fig. 18: Residence time of clouds of large spheres (1.00–2.80 mm in diameter) with different porosity. Porosity of spheres was higher for 1% agarose spheres (blue) than 2% agarose spheres (red). The total weight of each cloud was 8–10 g (25% of spheres and 75% of TL water (w/w)). The size range of each cloud was 1.00–1.40, 1.40–1.70, 1.70–2.00, 2.00–2.36, 2.36–2.80 mm in diameter. τ_r of single sphere experiment are also plotted for comparison (yellow and dark grey).

For large-sphere clouds, τ_r/τ_s has a power law relationship with the median size of spheres in the clouds (figure 19). It is also true for τ_r/τ_s of single spheres, and it seems that the relationship between τ_r/τ_s and sphere size is similar among the single sphere settling and the sphere cloud settling. The exponents (α, $\tau_r/\tau_s \sim \text{size}^\alpha$) lie between 2.427 and 2.699. Considering that diffusion time scale is proportional to size^2 (τ_d =size$^2/2D$), the experimental results shows that unknown processes, which further prolong τ_r, in addition to molecular diffusion might be involved. It is likely to be an influence of the entrained shell of TL fluid around a sphere, because it works as a barrier which slows down the diffusive exchange of salt by decreasing the gradient of salt at the surface of a sphere. Kindler *et al.* (2010) found the empirical relationship between residence time ($\tau_r{}^*$) and sphere size is $\tau_r{}^* \sim \text{size}^{2.1}$ ($\tau_r{}^*$ is Kindler *et al.*'s (2010) normalized residence time, $(\tau_r - \tau_s)/\tau_s$). Their α does not match with ours, and it would be due to the different experimental set up, e.g. the porosity and the solid matrix density of porous sphere and $\Delta\rho_f$. Nonetheless, their result still indicates processes other than diffusion would be involved in the settling of a porous particle.

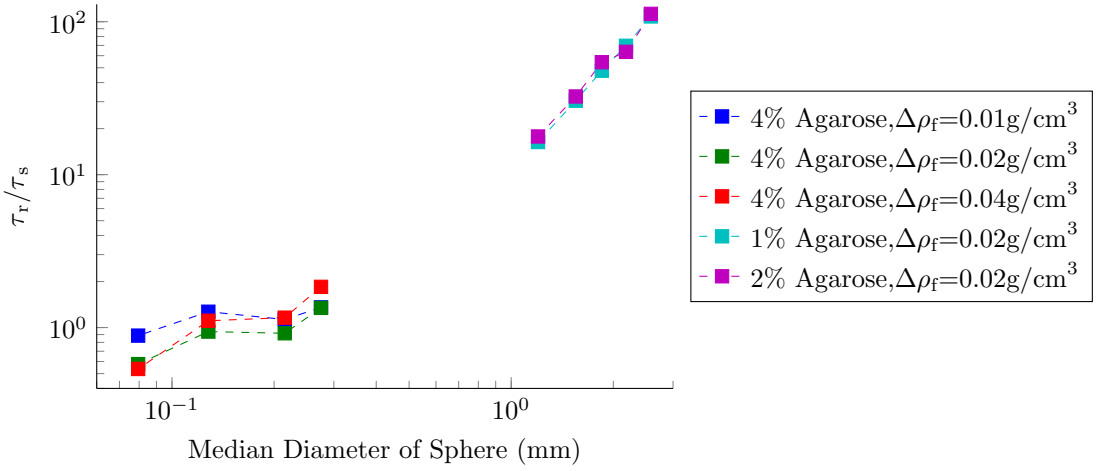

Fig. 19: Normalized residence time, τ_r/τ_s, of the clouds of spheres.

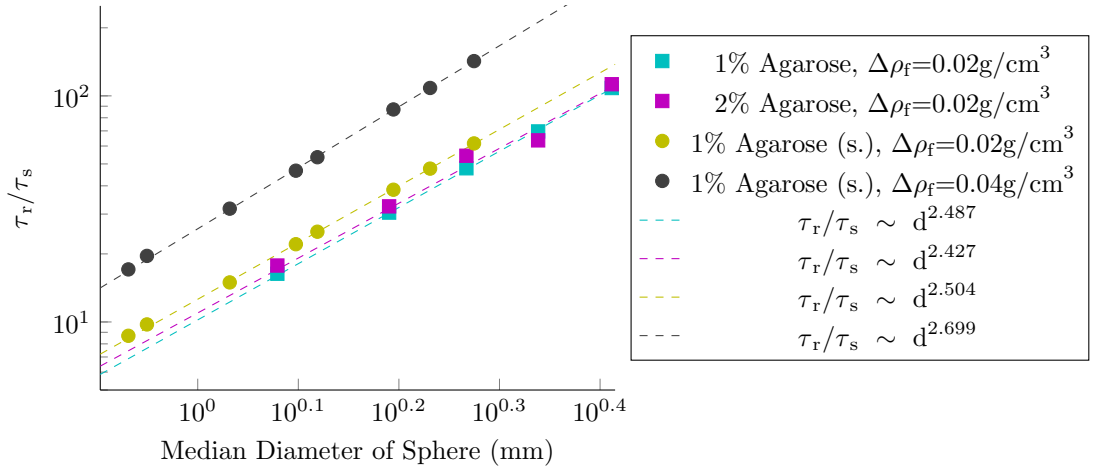

Fig. 20: Power-law fitting of τ_r/τ_s of the clouds of spheres. τ_r of the clouds of spheres (blue and red) and the single spheres (yellow and dark grey).

Both large- and small-sphere clouds seemed sensitive to the density slope of stratification, $d\rho_f/dz$, (figure 21), while small-sphere clouds were more sensitive. When $\Delta\rho_f$ was constant, τ_r was higher with smaller N^2. This might be due to the different thickness of the stratified region. When the stratification has a wider density interface or a smaller N^2, the time to settle through the stratified region is longer. Accordingly, small-sphere clouds, which are in the settling regime ($\tau_r/\tau_s \sim 1$ in figure 21 (b)), are more sensitive to the vertical extent of stratification than large-sphere clouds, which are in the diffusion regime.

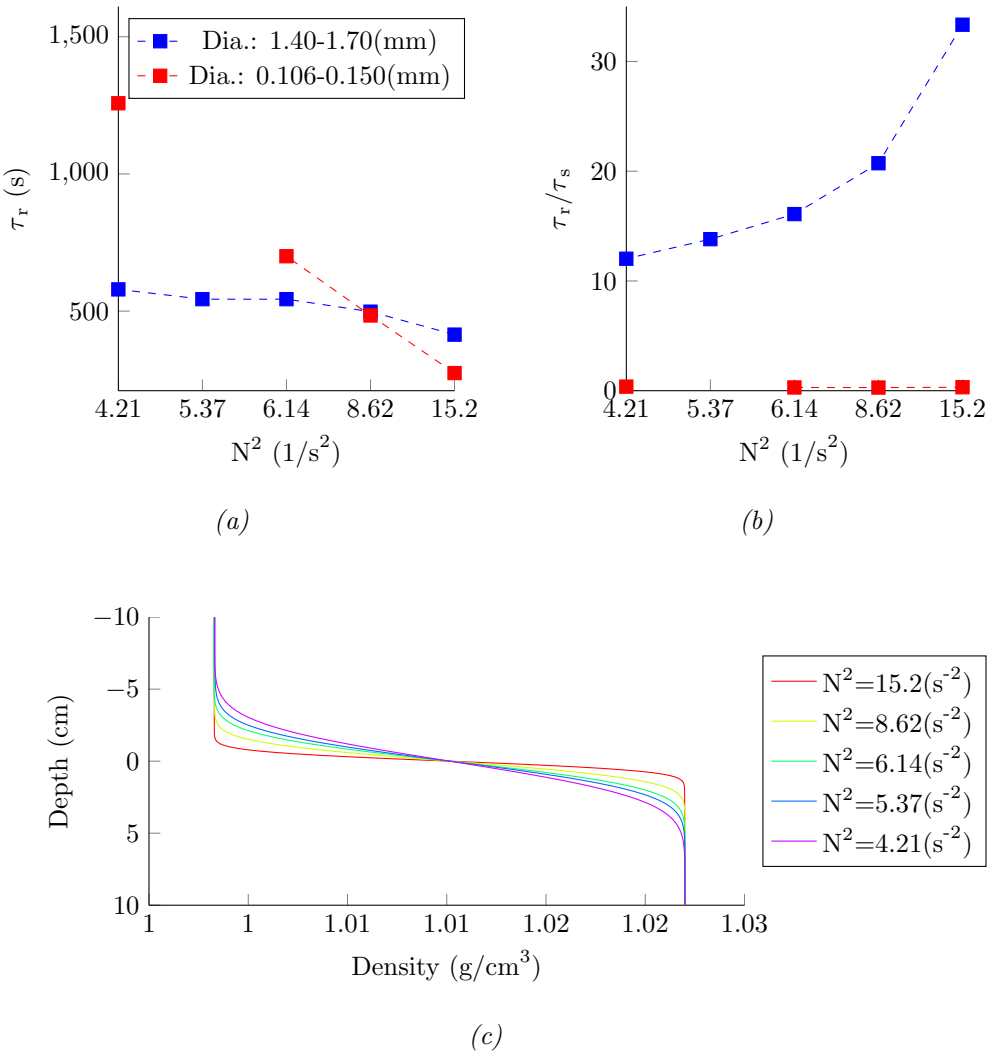

Fig. 21: τ_r of the clouds in different N^2. The dotted line in red shows τ_r (a) and τ_r/τ_s (b) from clouds of large spheres of 1% agarose, and the dotted line in blue shows a result from clouds of small spheres of 4% agarose in the five different stratifications (c). Releasing amount was 9.2g for a large sphere cloud and 1 cm^3 for a small sphere cloud, while the concentration of spheres in both clouds was identical (25% of spheres + 75% of TL water (w/w)). $\Delta\rho_f$ was $\sim$ 0.02 g/cm^3.

The numerical model of a porous sphere cloud was an ensemble of numerical simulation results of individual spheres (figure 22). The settling of individual spheres of various sizes with a uniform increment was simulated, and a sphere of each different size was weighted using a hypothetical size distribution. Then, the distribution of all spheres were recorded at every time step.

The cloud model result did not exactly match the experimental result (figure 22 (c)). First, the settling rate of the centroid in the actual experiment was initially faster than that of the model and decelerated in the top layer. This is due to turbulent entrainment (Scorer 1957; Noh & Fernando 1993; Bush *et al.* 2003). A cloud released with sufficient momentum gains a high velocity and accordingly generates turbulence, which eventually enhances mixing with ambient fluid. Through turbulent entrainment, the cloud grows while sinking, and its settling velocity

decreases since the initial momentum is diluted with entrained ambient fluid over time. However, the numerical model assumes every sphere in a cloud was initially at rest and accordingly had zero momentum. Hence, the numerical model result did not reproduce the same evolution of the sinking process.

Second, τ_r is significantly shorter in the numerical simulation result than in the experimental result (figure 23). The numerical model is an ensemble of results from single sphere settling model simulations, so it inherently has the same problem as the single sphere model—the absence of entrainment of lighter fluid from the top layer. However, it predicted the overall tendency of τ_r over the sphere size in clouds (figure 23).

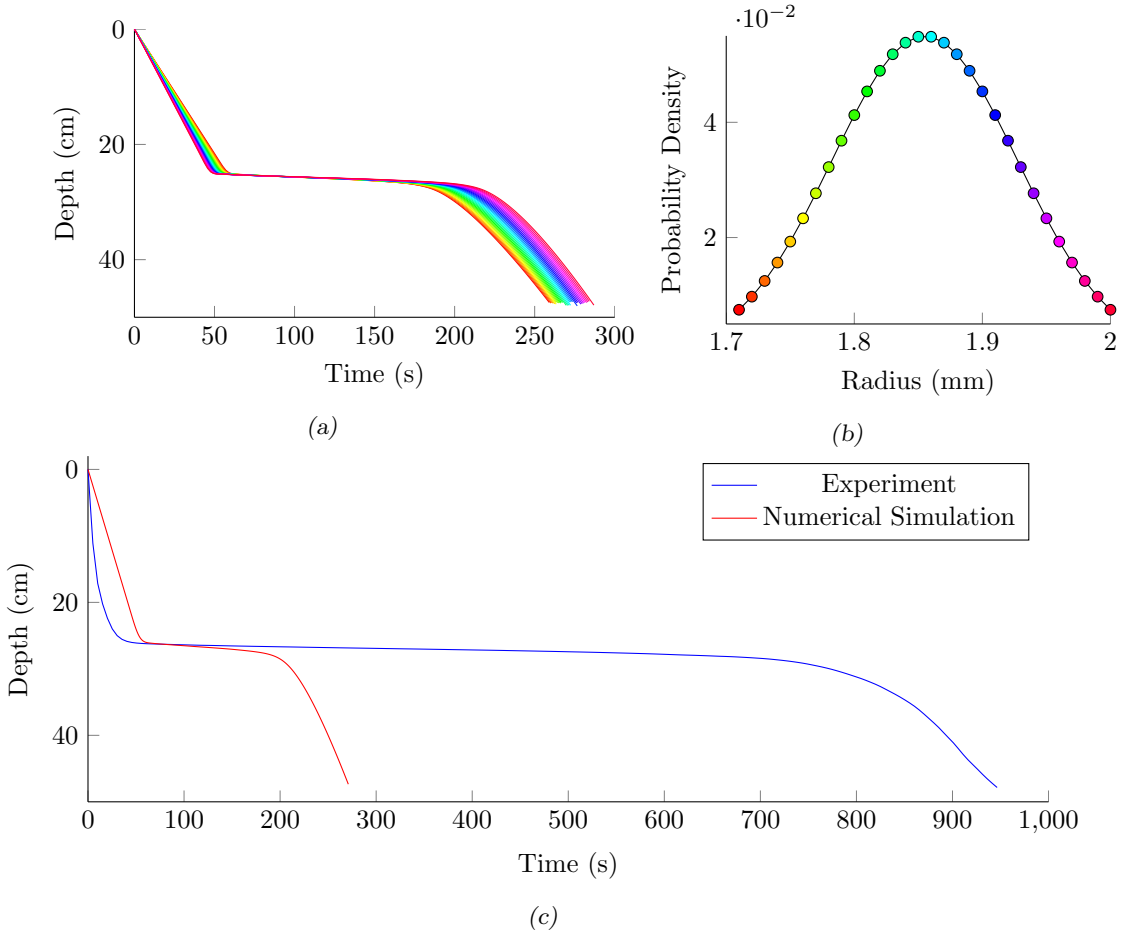

Fig. 22: Numerical simulation of a cloud of spheres. (a) Trajectories of individual spheres (d: 1.71–2.00 mm with 0.01 mm increment) from numerical simulation. The size distribution is shown on the right graph. Color scheme corresponds. (b) Size distribution (pdf) of spheres in a cloud. Normal distribution was assumed with $d_{mean} = d_{median}$ and $2\sigma = d_{median} - d_{min}$. (c) Comparison between experiment and numerical simulation. Experiment conditions were $\Delta\rho_f \cong 0.02 g/cm^3$, sphere size range: 1.70–1.20 mm, and releasing amount 10g (2.5g sphere + 7.5g TL water) as found in #10 in table 2.

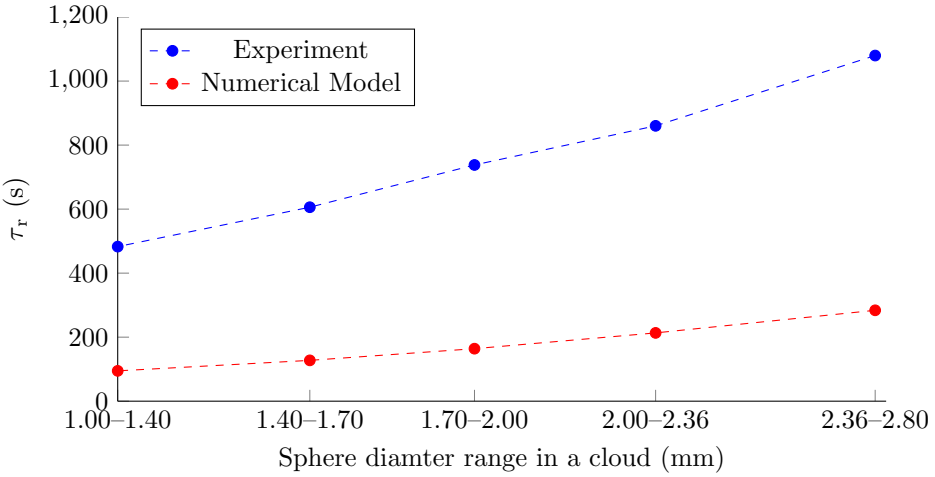

Fig. 23: Comparison between the experiment and numerical results of the clouds. Experimental conditions were $\Delta\rho_f \cong 0.02 g/cm^3$, sphere size range 1.70–2.00 mm, and releasing amount 10g (2.5g sphere + 7.5g TL water) as found in #10 in table 2.

In addition to the residence time of clouds, the evolution of cloud shapes over time was different between a small-sphere cloud and a large-sphere cloud (figure 24). Upon release, both clouds formed a turbulent thermal, but a small-sphere cloud seemed as if its thermal phase was terminated before reaching the density interface, while a large-sphere cloud was in a thermal phase when it hit the density interface. Accordingly, a large-sphere cloud arrives at the density interface faster than a small-sphere cloud (figure 27 (a-c)). Another big difference is the cloud shape at the density interface. Large-sphere clouds became very thin like a pancake, but small-sphere clouds were comparatively thicker at the density interface (figure 27 (d)).

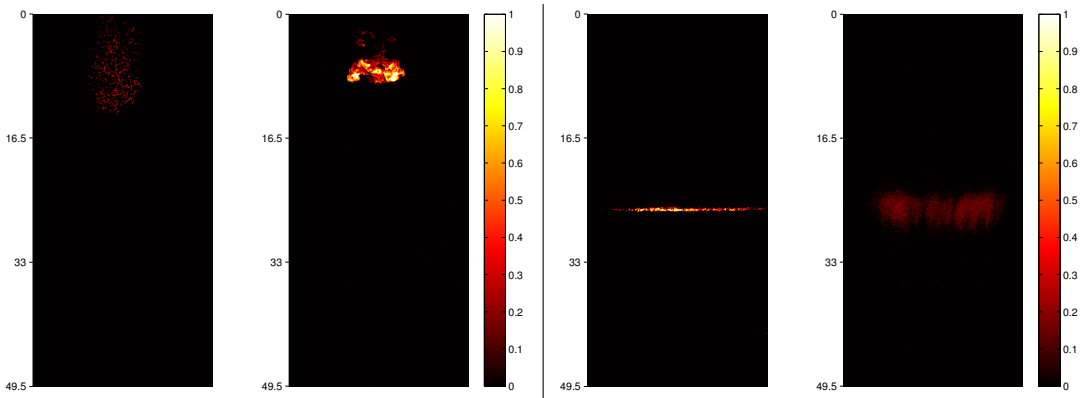

$(a) Z_c = 8(cm)$, $t_L = 2.15(s)$, $t_R = 23.5(s)$ $(d) Z_c = 26(cm)$, $t_L = 140(s)$, $t_R = 617(s)$

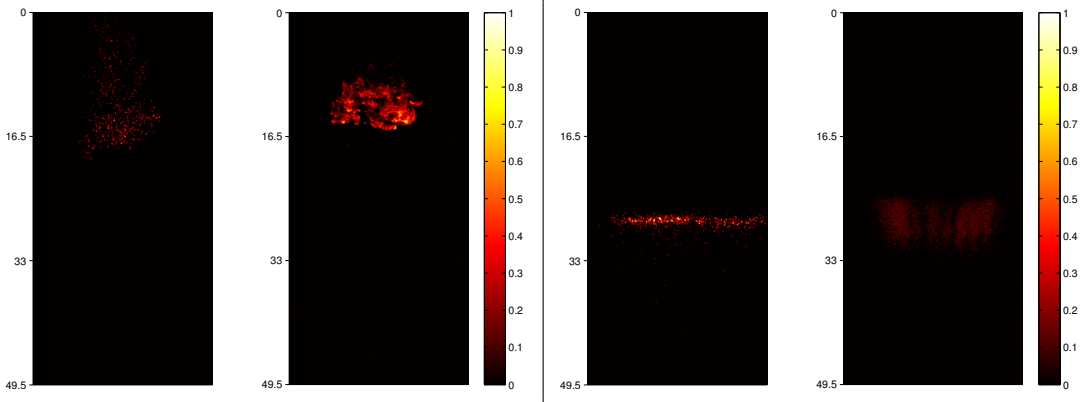

$(b) Z_c = 13(cm)$, $t_L = 5.57(s)$, $t_R = 51.5(s)$ $(e) Z_c = 26(cm)$, $t_L = 712(s)$, $t_R = 808(s)$

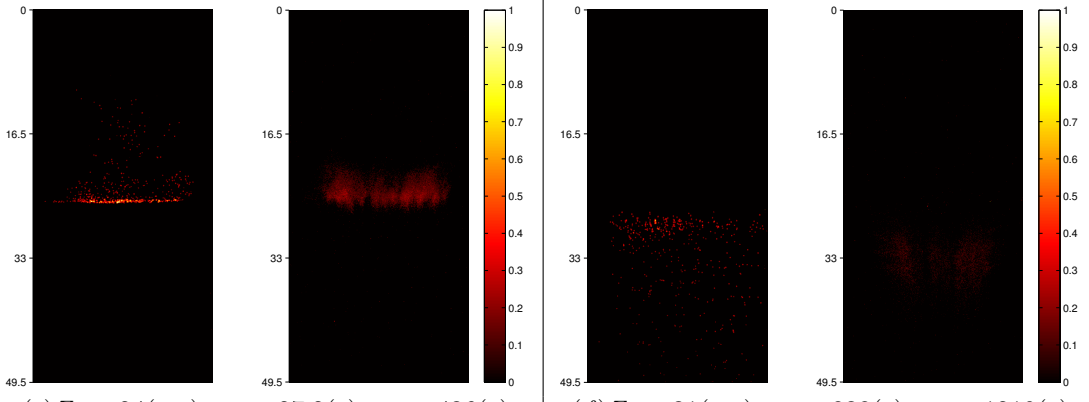

$(c) Z_c = 24(cm)$, $t_L = 27.2(s)$, $t_R = 436(s)$ $(f) Z_c = 31(cm)$, $t_L = 838(s)$, $t_R = 1210(s)$

Fig. 24: The comparison between a large-sphere cloud and a small-sphere cloud. Z_c: position of centroid, t_L: the record time for left pictures, and t_R: the record time for right pictures. In each pair of pictures, the left one is a cloud with 1.70–2.00 mm spheres, and the right one is a cloud with 0.106–0.150 mm spheres (more details are in table 2 #10 and #15). For better visualization, the intensity was amplified 1.5× and 3× respectively for large-sphere cloud and small-sphere cloud pictures.

To quantitatively investigate the evolution of cloud shapes, the standard deviation for vertical spread, the third standardized moment for vertical skewness, and the forth standardized moment for vertical kurtosis were calculated using equations (7–10) (figure 25). The vertical migration rate of a large-sphere cloud became nearly zero and it resided for a significant period of time at the density interface, while that of a small-sphere cloud decreased sharply at the density

interface, but not to zero. This is because the spheres in small- and large- sphere clouds are in different regimes—settling regime and diffusion regime, respectively.

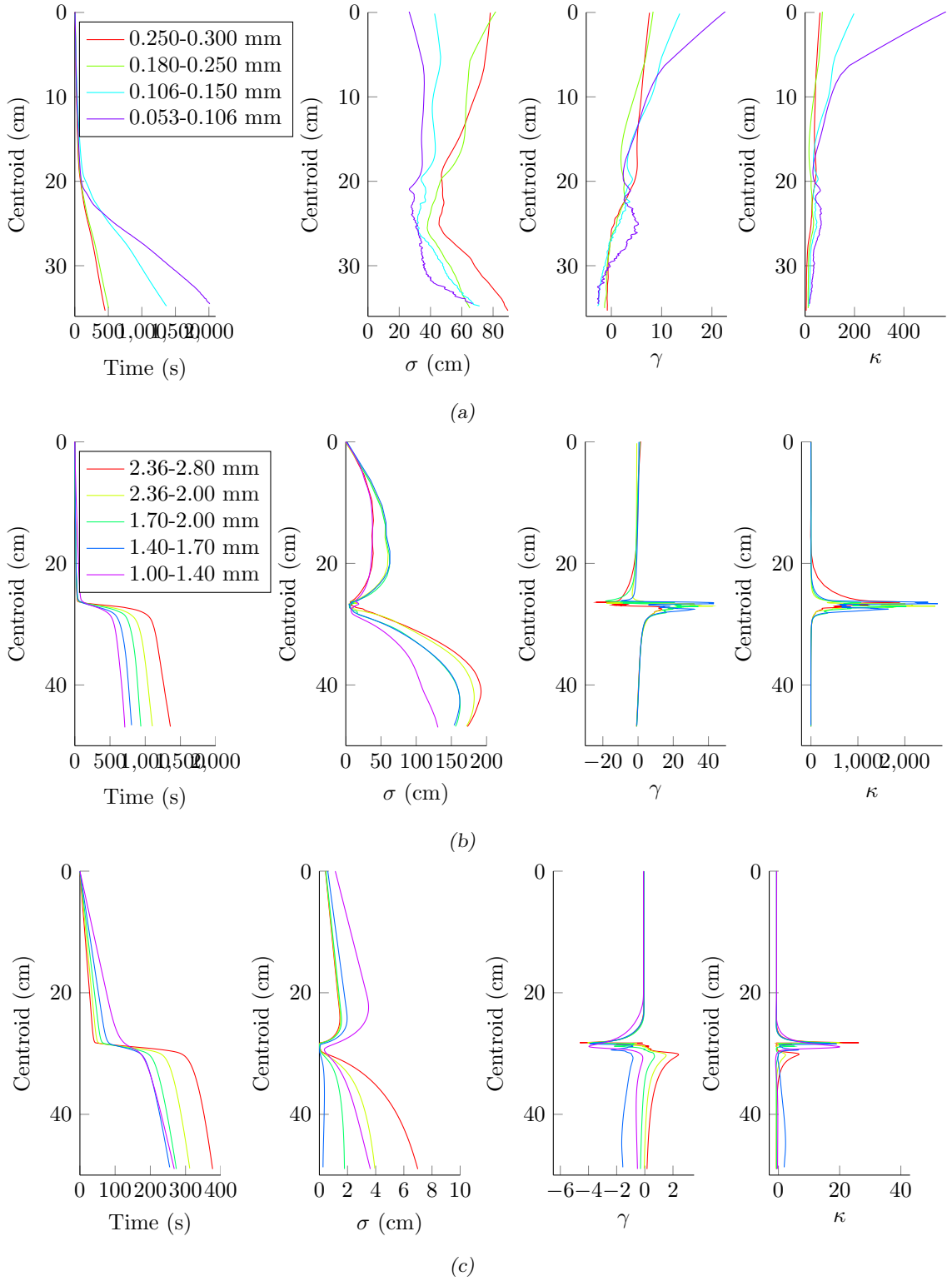

Fig. 25: Centroid (in the first column), standard deviation (in the second column), skewness (in the third column), and kurtosis (in the fourth column) of the clouds of spheres. *(a)* Small-sphere clouds (#14 in table 2). *(b)* Large-sphere clouds (#10 in table 2). *(c)* Large-sphere clouds (numerical simulation based on #10 in table 2).

The sphere clouds in different regimes show different spread, skweness, and kurtosis patterns. Both the small-sphere clouds and the large-sphere clouds show a tendency for their standard deviation to decrease until the centroid of the clouds reaches the density interfaces, then the standard deviation increases. However, the standard deviation of the large-sphere clouds decreases more sharply around the density interface and recovers faster in the bottom layer (figure 26), because the spheres in large-sphere clouds are pancaking with an extremely limited spread due to a prolonged diffusion time scale. This extreme pancaking causes the highest kurtosis and the smallest standard deviation at the density interface in figure 25. The pancaking can also explain the pattern of skewness of large-sphere clouds. In the TL, the frontmost spheres in a cloud start to be packed as soon as they reach the density interface; accordingly, they slow down while the rest of the spheres in the cloud is still sinking behind. This will make a negative tail or a negative skewness. Contrary to this, when the spheres escape the density interface, the frontmost spheres will accelerate to their terminal velocity in the bottom layer and sink faster while the rest of spheres are still trapped in the density interface. This will make a positive tail or a positive skewness.

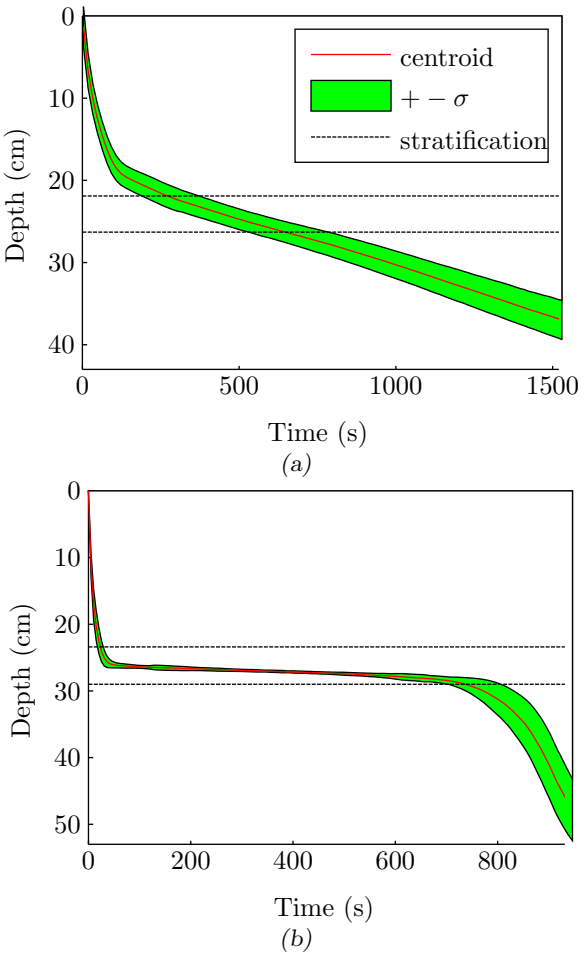

Fig. 26: Centroid and standard deviation of a cloud with 0.106–0.150 mm spheres (a) and 1.70–2.00 mm spheres (b) in 2-layer stratification ($\Delta\rho_f = 0.02$ g/cm^3). The stratified regions are within the two dotted lines. The red line is the centroid, and the green region shows the $\pm$ one standard deviation of the cloud.

On the other hand, the same pattern of the different moments was not observed in the small-sphere clouds, although their standard deviation was minimum around the density interface (figure 25 (a)). This is likely to be due to the absence of pancaking at the density interface. However, the slight decrease of standard deviation and the small increase of kurtosis around the density interface would indicate that the diffusive exchange of lighter interstitial fluid and denser ambient fluid still happens, although it is in a settling regime. The skewness of the small-sphere clouds generally decreases over depth.

The moments of a large-sphere cloud from the numerical model showed patterns similar to the experimental result although the magnitude of the higher moments were not captured well (figure 25 (c)). Both clouds show the extreme pancaking at the density interface (figure 27 (c) and (d)). This causes the smallest standard deviation and the largest kurtosis for the entire period of cloud growth. In addition, when both clouds leave the density interface, the clouds becomes positively skewed as smaller spheres start to settle earlier than larger ones (figure 27

((e) and (f)). However, a main difference is their behavior at the early stage. The cloud model does not demonstrate the thermal phase (figure 27 (a) and (b)). Due to the thermal phase, the large-sphere cloud from experiment stretches over a wide depth quickly upon its release, and this ultimately leads to a larger standard deviation than in the numerical simulations.

$d = 1.70 - 2.00(mm)$

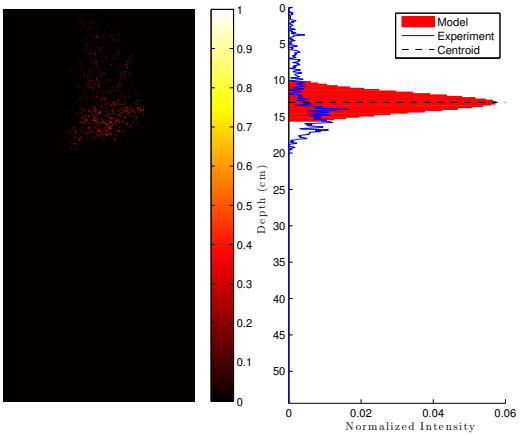

$(a) Z_c = 13(cm)$, $t_m = 26.9(s)$, $t_{exp} = 5.6(s)$

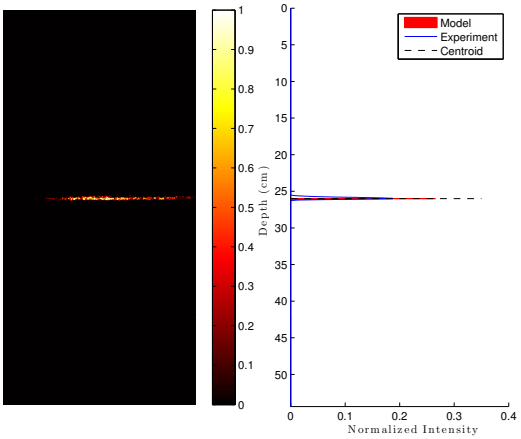

$(c) Z_c = 26(cm)$, $t_m = 105.3(s)$, $t_{exp} = 140.1(s)$

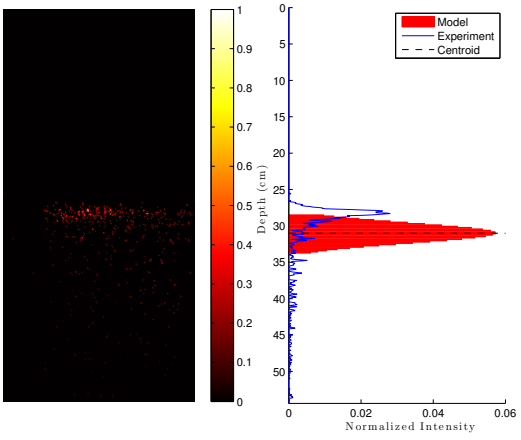

$(e) Z_c = 31(cm)$, $t_m = 218.6(s)$, $t_{exp} = 808.1(s)$

$d = 2.36 - 2.80(mm)$

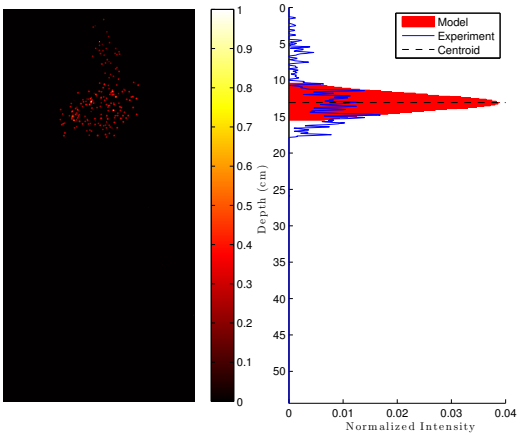

$(b) Z_c = 13(cm)$, $t_m = 41.8(s)$, $t_{exp} = 7.97(s)$

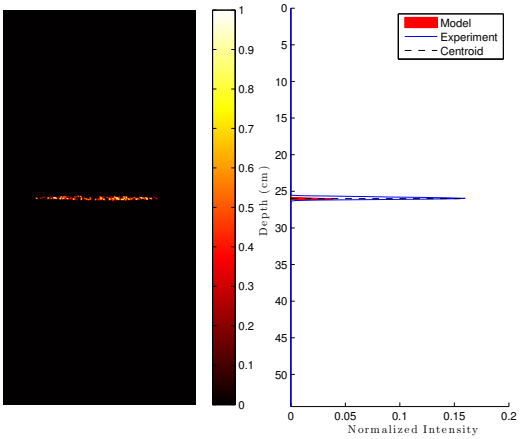

$(d) Z_c = 26(cm)$, $t_m = 91.0(s)$, $t_{exp} = 139.2(s)$

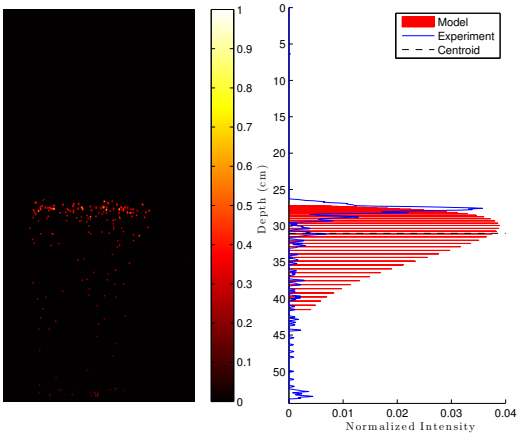

$(f) Z_c = 31(cm)$, $t_m = 109.8(s)$, $t_{exp} = 1147(s)$

Fig. 27: The comparison of the cloud growth between the experiment and the numerical simulation. The results from experiment and numerical simulation were compared when both had same centroids. Accordingly, the time points of both do not match as they have different growth. The picture on the lefthand side is post-processed and the pseudo-color shows the normalized brightness. The graph on the righthand side is the horizontally summed intensity profiles, and the values were normalized to make the area under the curve unity. The size range of sphere in the cloud was 1.70–2.00 mm (a, c, e) and 2.36–2.80 mm (b, d, f) in diameter. Further details of the experimental setting can be found in #10 in table 2.

Discussion

Entrainment of fluid around a sphere

To test if entrainment can prolong the residence time of a settling sphere in stratified environment, numerical simulation was performed with a modified momentum equation. Assuming the thickness of entrained fluid shell is fixed during the settling of a sphere, the entrained fluid shell was added in inertia and reduced gravity terms in equation (2):

$$M^* \frac{dU}{dt} = -\frac{\pi}{8}\rho_f U^2 C_D d^2 + M^* g - \rho_f V^* g \tag{12}$$

where M^* is the total mass of sphere and entrained fluid, $\frac{\pi}{6}\rho_s d^3 + \frac{\pi}{6}\rho_f({d^*}^3 - d^3)$, V^* is the total volume of sphere and entrained fluid, $\frac{\pi}{6}\rho_f {d^*}^3$, and d^* is the outer diameter of entrained fluid shell (figure 28).

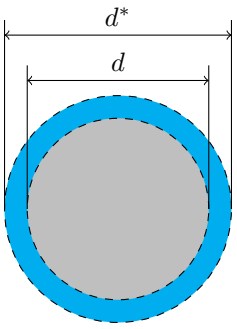

Fig. 28: A shell of entrained fluid around a sphere. A shell of entrained fluid (blue) wraps up a porous sphere (gray). d^* is an effective diameter of the settling sphere with a diameter of d.

In the modified numerical simulation, a porous sphere with an entrained fluid shell stayed longer within a stratified zone (figure 29 and figure 31). A larger entrained shell made τ_r larger for all spheres; however, the normalized thickness of an entrained fluid shell ($(d^* - d)/d$), which matches τ_r from laboratory experiment, decreases with the size of a sphere in the 2-layered stratification (e.g. τ_r of the smallest sphere from laboratory experiment lies between that from numerical simulation with $d^* = 1.4d$ and $d^* = 1.5d$, while τ_r of the largest sphere from laboratory experiment lies between that from numerical simulation with $d^* = 1.2d$ and $d^* = 1.3d$ in figure 30). However, in the linear stratification, it does not decrease monotonically with a sphere size, but increase with a sphere size and then decrease beyond a certain sphere size (figure 32).

It seems that size of a sphere is an important parameter to determine the thickness of an entrained fluid shell. It is possibly due to the fact that a faster flow around a larger sphere lessens the thickness of a boundary layer. Accordingly, the settling velocity of a sphere, not the

size of sphere which is one of important variables determining settling velocity, can be directly related to the thickness of the entrained fluid shell. In such a case, the thickness of an entrained fluid shell will be adjusted according to the settling velocity of the sphere. This needs further investigation since it contradicts the assumption of the fixed thickness of the entrained fluid shell.

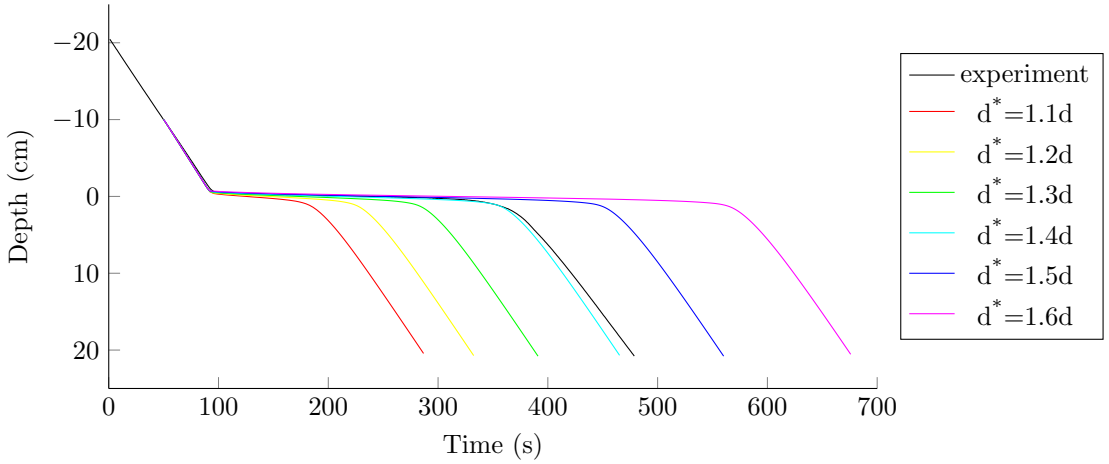

Fig. 29: Vertical trajectories of a agarose sphere with diameter, 0.1076 cm, from laboratory experiment (black) and numerical simulation with different entrained fluid shell thicknesses (colored). The experiment was performed in the 2-layered water column ($\Delta\rho_f$ = 0.02 g/cm^3, #6 in table 2). The numerical simulation was performed with a stratification and a sphere size identical to the experiment condition.

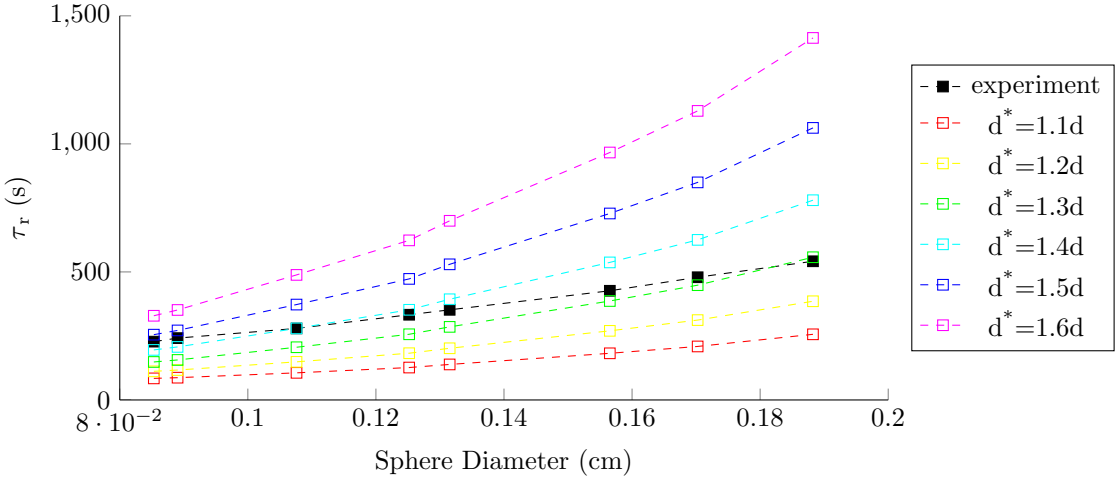

Fig. 30: τ_r of a agarose sphere from laboratory experiment (black) and numerical simulation with different entrained fluid shell thicknesses (colored). The experiment was performed with eight agarose spheres (table 3) in the 2-layered water column ($\Delta\rho_f$ = 0.02 g/cm^3, #6 in table 2). The numerical simulation was performed with a stratification and a sphere size identical to the experiment condition.

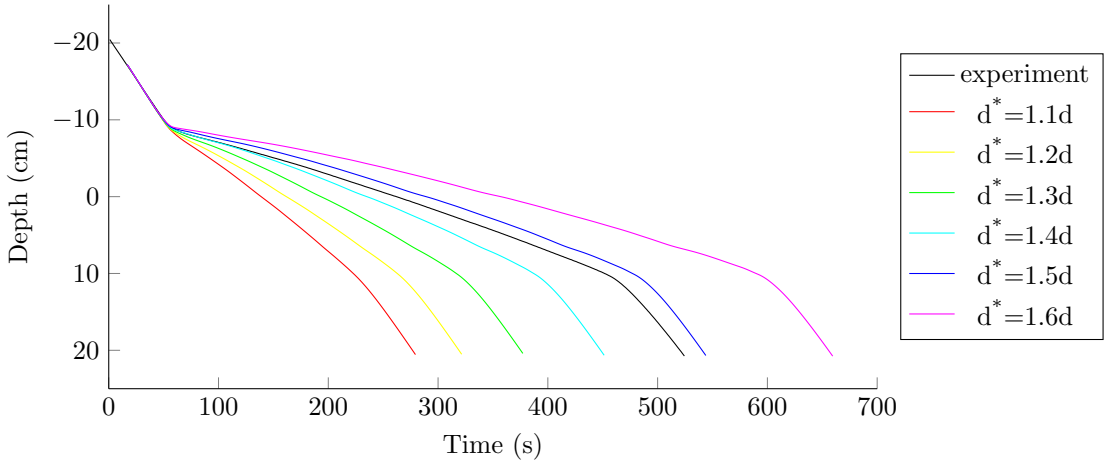

Fig. 31: Vertical trajectories of a agarose sphere with diameter, 0.1076 cm, from laboratory experiment (black) and numerical simulation with different entrained fluid shell thicknesses (colored). The experiment was performed in the linear water column ($\Delta\rho_f$ = 0.02 g/cm^3, #8 in table 2). The numerical simulation was performed with a stratification and a sphere size identical to the experiment condition.

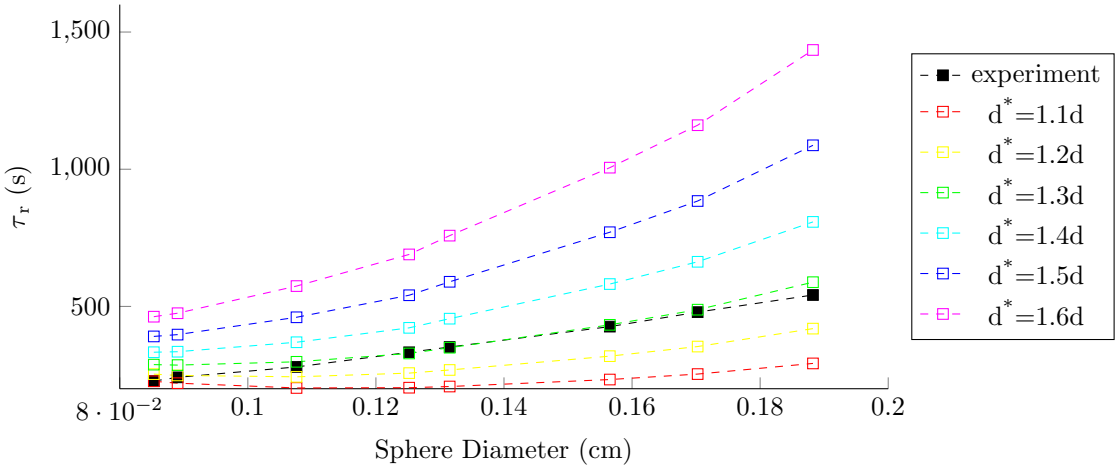

Fig. 32: τ_r of a agarose sphere from laboratory experiment (black) and numerical simulation (colored). The experiment was performed with eight agarose spheres (table 3) in the linear water column ($\Delta\rho_f$ = 0.02 g/cm^3, #8 in table 2). The numerical simulation was performed with a stratification and a sphere size identical to the experiment condition.

The settling velocity in both the top and bottom layers increases when the entrainment of a fluid shell is included (e.g. compare the black and blue lines in figure 29). This would be resulted from our rough assumption about entrainment, but it might be attributed to the way that the entrainment was incorporated in the momentum equation. In equation (12), the entrainment was introduced to the inertia and buoyancy terms, but not to the drag term.

V-shaped trend of τ_r

The v-shaped trend of τ_r was observed in numerical simulation of a single sphere settling (figure 14) and laboratory experiment of a sphere cloud settling (figure 16). This is because τ_r

can be roughly interpreted as the sum of the settling time scale, τ_s and the diffusion time scale, τ_d (defined as $a^2/2D$) (figure 33). In the numerical simulation with zero entrainment, when the spheres were very small, the τ_r was exactly identical to τ_s because τ_d was comparatively negligible. However, when the spheres were large, the trend of τ_r was dictated by that of τ_d, but the values of τ_r and $(\tau_d + \tau_s)$ did not match. This would be due to the simple representation of τ_d and the exclusion of the entrainment of lighter fluid in the vicinity of a sphere (Srdic-Mitrovic *et al.* 1999; Abaid *et al.* 2004; Camassa *et al.* 2009; Yick *et al.* 2009; Camassa *et al.* 2010). Nonetheless, the shift in dominant physical phenomena controlling τ_r over the sphere size range can be observed. The transition point between the settling regime ($\tau_r \sim \tau_s$) and the diffusion regime ($\tau_r \sim \tau_d$) lies somewhere around the sizes where $\tau_s = \tau_d$. It seems that, in a given water column depth and a given stratification, neither a very small nor very large particle stays the shortest time in the ocean, but some particle size in the middle does.

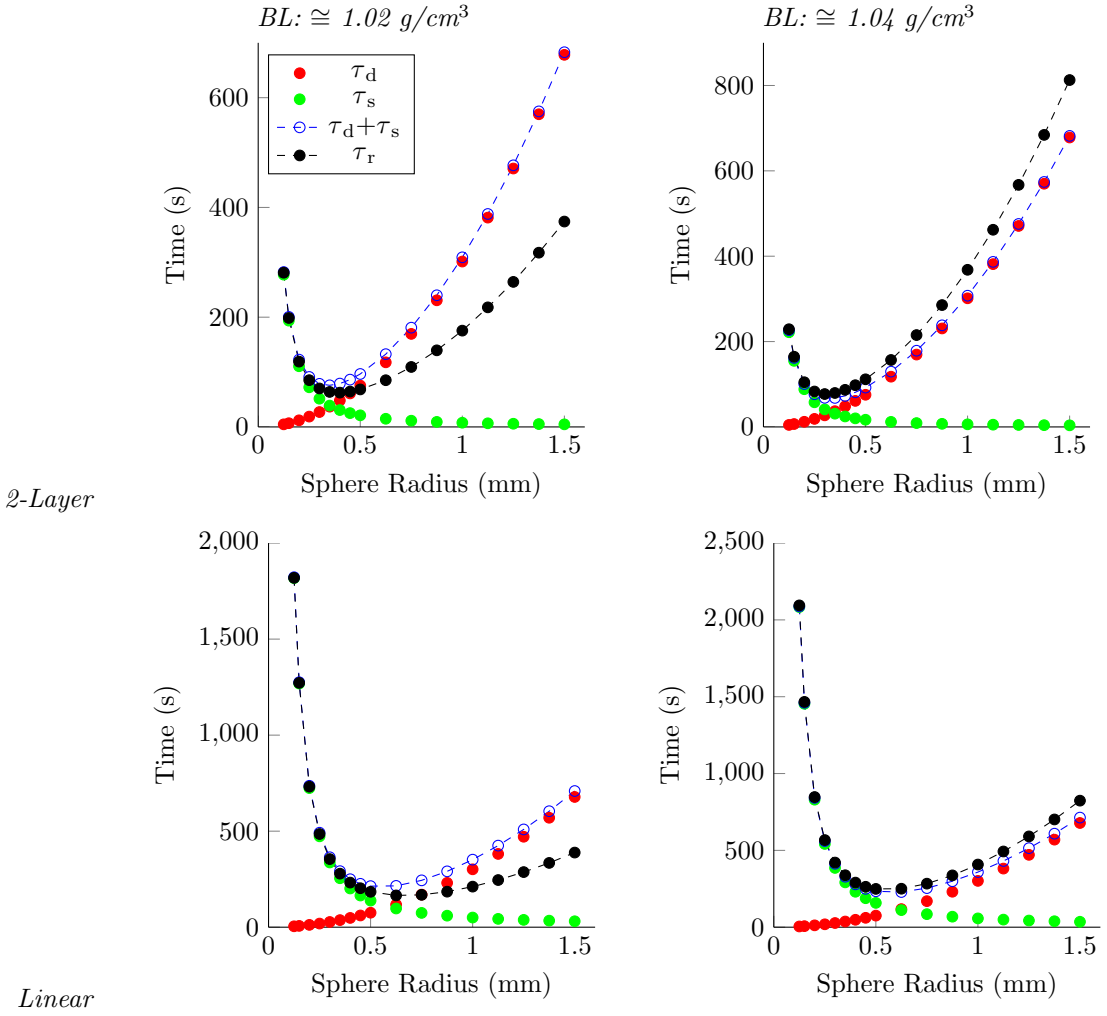

Fig. 33: Comparison between τ_r, diffusion time scale (τ_d), and settling time scale (τ_s) in 2-layer stratification (top) and linear stratification (bottom). The density difference between top and bottom layers ($\Delta\rho_f$) is ~ 0.02 g/cm^3 (left) and ~ 0.04 g/cm^3 (right). $\tau_d = \frac{a^2}{2D}$ and $\tau_s = l_{box}/w_s$.

τ_r/τ_s of a clouds of spheres from the laboratory experiment generally increases with the size range of spheres in the cloud (figure 19). The trend agrees well with the result of the single sphere numerical simulation (see red dots in figure 33). However, while τ_r/τ_s of a single sphere from numerical simulation is always larger than 1 (> 1.007), that of small-sphere clouds from laboratory experiment are in the range of 0.54–1.85. The value of smaller-than-unity τ_r/τ_s would be artifact due to the normalization using a settling time of a single sphere—τ_r of a cloud of spheres was calculated using its centroid, although that of a single sphere was calculated using its actual position. In addition, the value of smaller-than-unity τ_r/τ_s might be partly attributed to the overly simplified scaling of τ_s, just using two terminal velocities in the top and bottom layers.

Thin layer formation

Thin layers are the patches of marine particles including phytoplankton and marine snow within a limited vertical extent (e.g. less than 5 meters) above a certain concentration of particles (e.g. 2–3 times higher than the background concentration) (Dekshenieks *et al.* 2001; Sullivan *et al.* 2010). The fine-scale phenomena has been observed in various locations thanks to the recent progress in detection instruments and techniques, and the mechanisms of thin layer formation has been suggested (Durham & Stocker 2012). Considering thin layers are often associated with pycnocline in the ocean (Dekshenieks *et al.* 2001; Alldredge *et al.* 2002; Prairie *et al.* 2010), the delayed settling of porous spheres at stratification in this study can be one of possible scenarios related to the formation and dissipation of thin layers.

We found that a cloud of spheres are packed within a density interface for both small- and large-sphere clouds (figure 24). While the large-sphere clouds showed very thin layers within an extremely limited vertical range, the small spheres showed relatively thicker layers at the density interface. However, in both cases, the smallest vertical standard deviations of the sphere distributions were observed around density interfaces (figure 25). For large-sphere clouds, molecular diffusion of salt between the ambient and interstitial fluids drives the retention of spheres at density interfaces, and the entrained lighter fluid around sphere enhances the retention. However, for small-sphere clouds, molecular diffusion seems to be less important than the entrainment of lighter fluid. MacIntyre *et al.* (1995) hypothesized that marine aggregates would, at density stratification, accumulate due to the time to equilibrate the interstitial fluid density with the ambient fluid density. Although, Kindler *et al.* (2010); Prairie *et al.* (2012) demonstrated the prolonged retention of porous spheres and real aggregates, respectively, by laboratory experiment, this study showed the prolonged retention of multiple particles, which is more similar to the oceanic situation of thin layer formation.

The laboratory experiments and numerical simulations in this study were conducted in stratifications with $\Delta\rho_f = O(10^{-2} g/cm^3)$, which is an order of magnitude higher than stratification of open sea. Accordingly, the retention of spheres within such a weak stratification would be different from that of this study. However, environment similar to the experimental condition in this study can be found in stratified estuaries (MacDonald & Horner Devine 2008; Kasai *et al.* 2010). Even more extreme stratifications are also found in the ocean. The density interface of brine pools have stratification with $\Delta\rho_f = O(10^{-1} g/cm^3)$ (Shokes *et al.* 1977; Eder *et al.* 2001). In these cases, the settling behavior of marine porous particles might be comparable to the result of this study.

Conclusions

Through experimental and computational work, the settling behavior of both an individual porous sphere and a cloud of porous spheres in different stratified environments was investigated. The porosity of spheres and the presence of density stratification introduce unique settling behavior compared to a non-porous sphere settling. For example, if the density of a non-porous sphere is between those of TL fluid and BL fluid, it will be stuck in the density interface as long as the stratification persists. However, if it is a porous sphere, it will eventually escape the density interface after gaining excess density through diffusive exchange between the sphere's lighter interstitial fluid and the denser ambient fluid. Therefore, the time scale of delayed settling in the stratified region is of key interest in this study. Residence time (τ_r) was used to measure the delayed settling. τ_r is defined as the time taken to settle through a stratified region, which is defined by density gradient $\frac{d\rho_f}{dz} \geq 0.001(\frac{d\rho_f}{dz})_{max}$, (figure 8 (c) and (d)).

The τ_r of a single sphere decreases with its size when the sphere is smaller than a certain size (settling regime). However, when the sphere is larger than that size, τ_r increases with its size (diffusion regime). Accordingly, it forms a v-shaped curve if τ_r to the size of sphere is plotted (figure 14). This is because the time scale of delayed settling, τ_r, is mainly governed by settling processes and molecular diffusion. Therefore, these time scales can be considered roughly as a sum of the settling time scale (τ_s) and the diffusion time scale (τ_d) (figure 33). If the size of the sphere is the same, τ_r increases with $\Delta\rho_f$ (figure 9). If $\Delta\rho_f$ is the same, τ_r was longer in a linear stratification than in a sharp 2-layered stratification (figure 10).

A similar v-shaped trend was observed in the settling of a cloud of porous spheres (figure 16). Also, τ_r increased with $\Delta\rho_f$ and porosity (figure 17 and figure 18). In a 2-layer environment, τ_r

of small-sphere clouds was longer with smaller N^2 (figure 21). In addition to τ_r, the evolution of cloud shapes was studied (figure 24–27).

Before including the entrainment of a fluid shell, the numerical simulation results for both a single sphere and a sphere cloud did not exactly match the experimental results (figure 11 and 22 (c)). The τ_r from the numerical model were smaller than the experimental result in all cases (figure 13 and 23). However, the model could predict the tendency of τ_r, e.g. the v-shaped trend (figure 14). Specifically for a cloud of spheres, the vertical migration rate of the centroid of a cloud in the top layer was slower in the numerical model than in the experiments, since the initial turbulent thermal phase was not included in the model (figure 22(c)).

The modified numerical model, which included the shell of entrained fluid in our model (figure 28), predicted τ_r better than the original model for a single sphere settling. The thickness of entrained fluid shell seemed to vary over the size of spheres (figure 30 and figure 32). However, our assumption that the entrained fluid shell thickness does not change during settling needs to be investigated further. Although the cloud model simulation with entrainment was not conducted, it is very likely that τ_r of sphere clouds will also increase in the numerical model with entrainment because the cloud model is the ensemble of single sphere model simulation results.

The delayed settling of porous spheres in the stratified region would be a possible mechanism of thin layer formation in the ocean. Previously, a hypothesis was proposed that marine porous aggregates might accumulate at the stratified region due to the time taken for density equilibration (MacIntyre *et al.* 1995). Also, some laboratory experiments, which can support the hypothesis, were performed using porous spheres and real aggregates (Kindler *et al.* 2010; Prairie *et al.* 2012). However, we showed the prolonged accumulation of a cloud of porous spheres at the density interface, which is more similar to thin layers in nature.

In order to understand the settling problem better, the following work needs to be done. First, further laboratory experiments, which were not conducted due to the technical issues, will enhance our knowledge. Single sphere settling experiments for very small spheres (< 0.8 mm diameter) will let us find the transition point where the dominant regime (diffusion vs. settling) changes. Also, cloud settling experiments in a linear stratification will let us know if τ_r is longer in a linear stratification than in a 2-layer stratification. Third, the numerical model needs to be improved especially for the estimation of the entrained fluid shell thickness and the incorporation of the entrainment fluid shell into the numerical model.

Most importantly, the outcome of this study must be compared to the real marine snow. Although the agarose spheres in this study had a high porosity (> 99 %), as marine snow does, real marine snow characteristics, including porosity, solid matrix density, and shape, are highly

variable. In addition, the stratification in most parts of the ocean is orders of magnitude smaller than that in our study, although a certain environment, which our study result can be directly applied to, exists (e.g. stratified estuaries and brine pools). Accordingly, experimentation with real marine snow will give us a better idea how this study can be calibrated so that it can be further used to investigate the settling behavior of marine snow.

Appendix

A. Skewness and kurtosis

Skewness is a measure of asymmetry of a distribution. If a distribution has a positive skewness, it has a longer tail on the right side than that on the left side, and its mass lies more on the left side. On the other hand, if a distribution has a negative skewness, it has a longer tail on the left side than that on the right side, and its mass lies more on the right side. The third standardized moment is commonly used for a measure of skewness:

$$\text{Skewness} = \frac{\sum_{i=1}^{N}(x_i - \mu)^3}{(N-1)\sigma^3}$$

where N is the sample size, x_i is the value of the i_{th} sample, μ is the mean, and σ is the standard deviation.

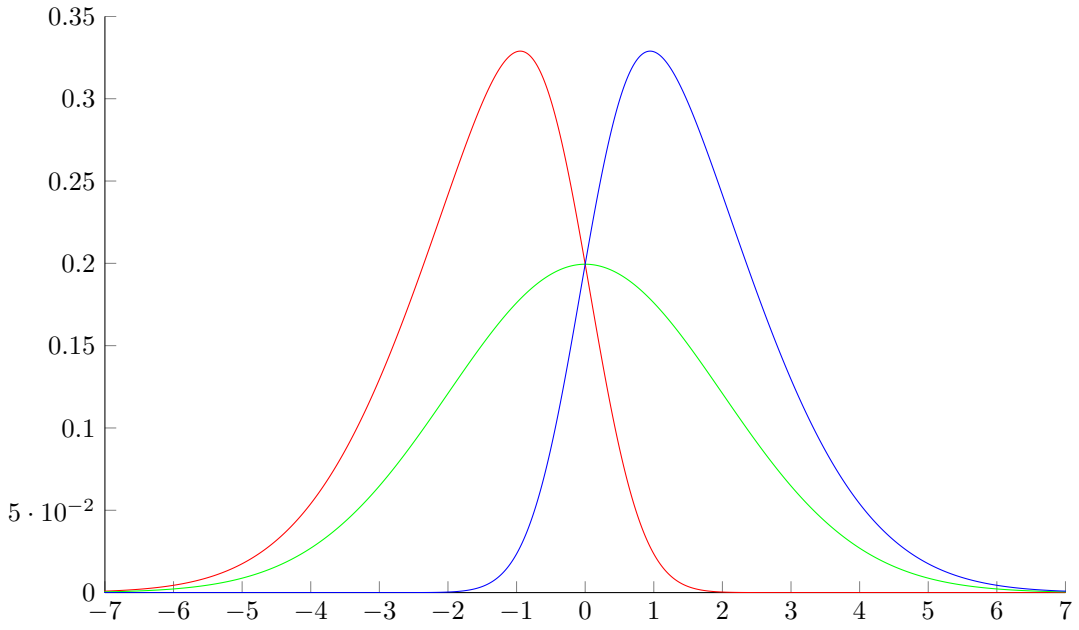

Fig. 34: Probability distributions with zero skewness (green), a negative skewness (red), and a positive skewness (blue).

Kurtosis is a measure of how peaked a distribution is compared to a normal distribution. If a distribution has a high kurtosis, it has a sharper peak around its mean with a fatter tail compared to a normal distribution. On the other hand, if a distribution has a low kurtosis, it has a blunter peak around its mean with a thinner tail compared to a normal distribution. The fourth standardized moment is comonly used for a measure of kurtosis:

$$\text{Kurtosis} = \frac{\sum_{i=1}^{N}(x_i - \mu)^4}{(N-1)\sigma^4}$$

. A normal distribution has a kurtosis of 3; therefore, a distribution with a kurtosis higher (or lower) than 3 is more peaked (or less peaked) than a normal distribution.

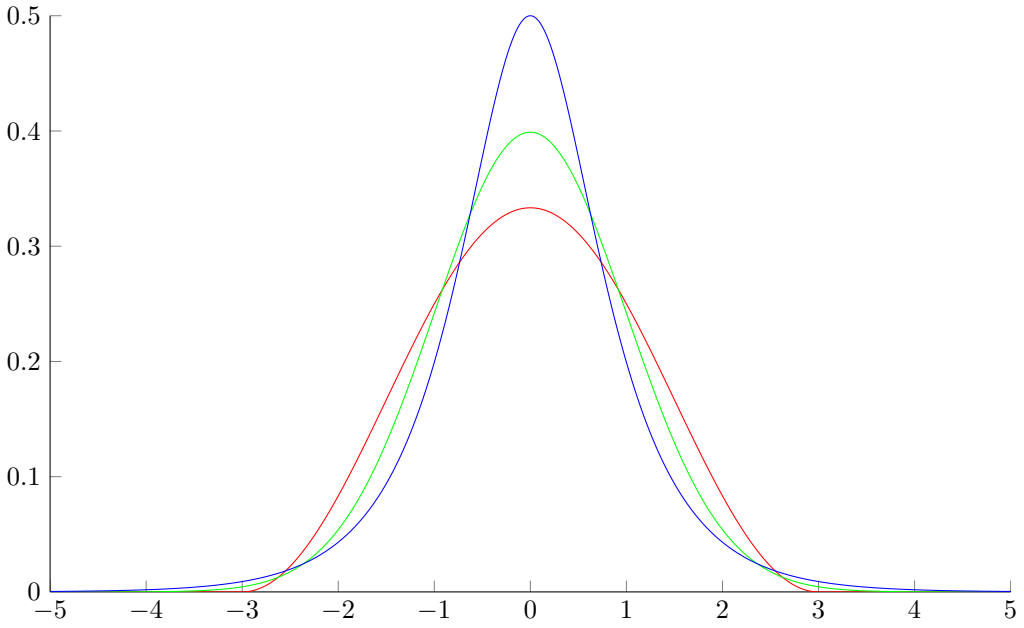

Fig. 35: Probability distributions with a kurtosis of 3 (green), a kurtosis smaller than 3 (red), and a kurtosis higher than 3 (blue).

B. NaCl concentration–density conversion table

(Source: Mettler Toledo, http://us.mt.com/us/en/home/supportive_content/application_editorials/Sodium_Chloride_de_e.html).

[NaCl] (% by wt.)	Density (g/cm^3)
0.10	0.9989
0.20	0.9997
0.30	1.0004
0.40	1.0011
0.50	1.0018
0.60	1.0025
0.70	1.0032
0.80	1.0039
0.90	1.0046
1.00	1.0053
1.10	1.0060

[NaCl] (% by wt.)	Density (g/cm^3)
1.20	1.0068
1.30	1.0075
1.40	1.0082
1.50	1.0089
1.60	1.0096
1.70	1.0103
1.80	1.0110
1.90	1.0117
2.00	1.0125
2.10	1.0132
2.20	1.0139
2.30	1.0146
2.40	1.0153
2.50	1.0160
2.60	1.0168
2.70	1.0175
2.80	1.0182
2.90	1.0189
3.00	1.0196
3.10	1.0203
3.20	1.0211
3.30	1.0218
3.40	1.0225
3.50	1.0232
3.60	1.0239
3.70	1.0246
3.80	1.0254
3.90	1.0261
4.00	1.0268
4.10	1.0275
4.20	1.0282
4.30	1.0290

[NaCl] (% by wt.)	Density (g/cm^3)
4.40	1.0297
4.50	1.0304
4.60	1.0311
4.70	1.0318
4.80	1.0326
4.90	1.0333
5.00	1.0340
5.20	1.0355
5.40	1.0369
5.60	1.0384
5.80	1.0398
6.00	1.0413
6.20	1.0427
6.40	1.0442
6.60	1.0456
6.80	1.0471
7.00	1.0486
7.20	1.0500
7.40	1.0515
7.60	1.0530
7.80	1.0544
8.00	1.0559
8.20	1.0574
8.40	1.0588
8.60	1.0603
8.80	1.0618
9.00	1.0633
9.20	1.0647
9.40	1.0662
9.60	1.0677
9.80	1.0692
10.00	1.0707

[NaCl] (% by wt.)	Density (g/cm^3)
10.50	1.0744
11.00	1.0781
11.50	1.0819
12.00	1.0857
12.50	1.0894
13.00	1.0932
13.50	1.0970
14.00	1.1008
14.50	1.1047
15.00	1.1085
16.00	1.1162
17.00	1.1240
18.00	1.1319
19.00	1.1398
20.00	1.1478
21.00	1.1558
22.00	1.1640
23.00	1.1721
24.00	1.1804
25.00	1.1887
26.00	1.1972

References

Abaid, N., Adalsteinsson, D., Agyapong, A. & McLaughlin, R. M. 2004 An internal splash: Levitation of falling spheres in stratified fluids. *Physics of Fluids* **16** (5), 1567.

Alldredge, A. L., Cowles, T. J., MacIntyre, S., Rines, J. E. B., Donaghay, P. L., Greenlaw, C. F., Holliday, D. V., Dekshenieks, M. M., Sullivan, J. M. & Zaneveld, J. R. V. 2002 Occurrence and mechanisms of formation of a dramatic thin layer of marine snow in a shallow Pacific fjord. *Marine Ecology Progress Series* **233**, 1–12.

Alldredge, A. L. & Gotschalk, C. 1988 In situ settling behavior of marine snow. *Limnology and Oceanography* pp. 339–351.

Alldredge, A. L. & Silver, M. W. 1988 Characteristics, dynamics and significance of marine snow. *Progress in Oceanography* **20** (1), 41–82.

Bühler, J. & Papantoniou, D. A. 2001 On the motion of suspension thermals and particle swarms. *Journal of Hydraulic Research* **39** (6), 643–653.

Burd, A. B., Hansell, D. A., Steinberg, D. K., Anderson, T. R., Arístegui, J., Baltar, F., Beaupre, S. R., Buesseler, K. O., DeHairs, F. & Jackson, G. A. 2010 Assessing the apparent imbalance between geochemical and biochemical indicators of meso-and bathypelagic biological activity: What the @$#! is wrong with present calculations of carbon budgets? *Deep Sea Research Part II: Topical Studies in Oceanography* **57** (16), 1557–1571.

Bush, J. W. M., Thurber, B. A. & Blanchette, F. 2003 Particle clouds in homogeneous and stratified environments. *Journal of Fluid Mechanics* **489**, 29–54.

Camassa, R., Falcon, C., Lin, J., McLaughlin, R. M. & Mykins, N. 2010 A first-principle predictive theory for a sphere falling through sharply stratified fluid at low Reynolds number. *Journal of Fluid Mechanics* **664**, 436–465.

Camassa, R., Falcon, C., Lin, J., McLaughlin, R. M. & Parker, R. 2009 Prolonged residence times for particles settling through stratified miscible fluids in the Stokes regime. *Physics of Fluids* **21** (3), 031702.

Dekshenieks, M. M., Donaghay, P. L., Sullivan, J. M., Rines, J. E. B., Osborn, T. R. & Twardowski, M. S. 2001 Temporal and spatial occurrence of thin phytoplankton layers in relation to physical processes. *Marine Ecology ...* .

Durham, W. M. & Stocker, R. 2012 Thin Phytoplankton Layers: Characteristics, Mechanisms, and Consequences. *Annual Review of Marine Science* **4** (1), 177–207.

Eder, W., Jahnke, L. L., Schmidt, M. & Huber, R. 2001 Microbial Diversity of the Brine-Seawater Interface of the Kebrit Deep, Red Sea, Studied via 16S rRNA Gene Sequences and Cultivation Methods. *Applied and Environmental Microbiology* **67** (7), 3077–3085.

Falkowski, P. 2000 The Global Carbon Cycle: A Test of Our Knowledge of Earth as a System. *Science* **290** (5490), 291–296.

Fowler, S. W. & Knauer, G. A. 1986 Role of large particles in the transport of elements and organic compounds through the oceanic water column. *Progress in Oceanography* **16** (3), 147–194.

Henson, S. A., Sanders, R., Madsen, E., Morris, P. J., Le Moigne, F. & Quartly, G. D. 2011 A reduced estimate of the strength of the ocean's biological carbon pump. *Geophysical Research Letters* **38** (4), L04606–.

Honjo, S., Manganini, S. J., Krishfield, R. A. & Francois, R. 2008 Particulate organic carbon fluxes to the ocean interior and factors controlling the biological pump: a synthesis of global sediment trap programs since 1983. *Progress in Oceanography* **76** (3), 217–285.

Iversen, M. & Ploug, H. 2010 Ballast minerals and the sinking carbon flux in the ocean: carbon-specific respiration rates and sinking velocity of marine snow aggregates. *Biogeosciences 7:* pp. 2613–2624.

Johnson, R. W., ed. 1998 *Handbook of fluid dynamics*. CRC Press LLC.

Kajihara, M. 1971 Settling velocity and porosity of large suspended particle. *Journal of Oceanography* **27** (4), 158–162.

Kasai, A., Kurikawa, Y., Ueno, M., Robert, D. & Yamashita, Y. 2010 Salt-wedge intrusion of seawater and its implication for phytoplankton dynamics in the Yura Estuary, Japan. *Estuarine, Coastal and Shelf Science* **86** (3), 408–414.

Khelifa, A. & Hill, P. S. 2006 Models for effective density and settling velocity of flocs. *Journal of Hydraulic Research* **44** (3), 390–401.

Kindler, K., Khalili, A. & Stocker, R. 2010 Diffusion-limited retention of porous particles at density interfaces. *Proceedings of the National Academy of Sciences* **107** (51), 22163–22168.

Kiørboe, T., Grossart, H., Ploug, H. & Tang, K. 2002 Mechanisms and Rates of Bacterial Colonization of Sinking Aggregates. *Applied and ...* **68** (8), 3996–4006.

Kranenburg, C. 1994 The fractal structure of cohesive sediment aggregates. *Estuarine, Coastal and Shelf Science* **39** (6), 451–460.

Laws, E. A., Falkowski, P. G., Smith, W. O. Jr, Ducklow, H. & McCarthy, J. J. 2000 Temperature effects on export production in the open ocean. *Global Biogeochemical Cycles* **14** (4), 1231–1246.

Luketina, D. & Wilkinson, D. 1994 *Particle clouds in density stratified environments*. ITG,

Grenoble.

MacDonald, D. G. & Horner Devine, A. R. 2008 Temporal and spatial variability of vertical salt flux in a highly stratified estuary. *Journal of Geophysical Research: Oceans (1978–2012)* **113** (C9).

MacIntyre, S., Alldredge, A. L. & Gotschalk, C. C. 1995 Accumulation of marine snow at density discontinuities in the water column. *Limnology and Oceanography* pp. 449–468.

McDougall, T. J. & Barker, P. M. 2011 *Getting started with TEOS-10 and the Gibbs Seawater (GSW) Oceanographic Toolbox*. SCOR/IAPSO WG127.

McManus, M. A., Kudela, R. M., Silver, M. W., Steward, G. F., Donaghay, P. L. & Sullivan, J. M. 2008 Cryptic blooms: Are thin layers the missing connection? *Estuaries and Coasts* **31** (2), 396–401.

Noh, Y. 2000 Sedimentation of a particle cloud across a density interface. *Fluid Dynamics Research* **27** (3), 129–142.

Noh, Y. & Fernando, H. J. S. 1993 The transition in the sedimentation pattern of a particle cloud. *Physics of Fluids A: Fluid Dynamics* **5**, 3049–3049.

Oster, G. 1965 Density gradients. *Scientific American* **213**, 70–76.

Prairie, J. C., Franks, P. J. S. & Jaffe, J. S. 2010 Cryptic peaks: Invisible vertical structure in fluorescent particles revealed using a planar laser imaging fluorometer. *Limnology and Oceanography* **55** (5), 1943.

Prairie, J. C., Ziervogel, K., Arnosti, C., Camassa, R., Falcon, C., Khatri, S., McLaughlin, R. M., White, B. L. & Yu, S. 2012 Delayed settling of marine snow. In *The 2nd International Workshop on Marine Aggregates from Molecular Principles to Biological Impact*, pp. 1–1. Bremen, Germany.

Rahimipour, H. & Wilkinson, D. 1992 Dynamic behaviour of particle clouds. In *Proc. 11th Australasian Fluid Mech Conf., Hobart, Australia*, pp. 743–746.

Scorer, R. S. 1957 Experiments on convection of isolated masses of buoyant fluid. *Journal of Fluid Mechanics* **2** (06), 583–594.

Shokes, R. F., Trabant, P. K., Presley, B. J. & Reid, D. F. 1977 Anoxic, hypersaline basin in the northern Gulf of Mexico. *Science* **196** (4297), 1443–1446.

Slack, G. W. 1963 Sedimentation of a large number of particles as a cluster in air. *Nature Publishing Group* **200**, 1306.

Srdic-Mitrovic, A. N., Mohamed, N. A. & Fernando, H. J. S. 1999 Gravitational settling of particles through density interfaces. *Journal of Fluid Mechanics* **381**, 175–198.

Sullivan, J. M., McManus, M. A., Cheriton, O. M., Benoit-Bird, K. J., Goodman, L., Wang, Z., Ryan, J. P., Stacey, M., Van Holliday, D., Greenlaw, C., Moline, M. A. & McFarland, M. 2010 Layered organization in the coastal ocean: An introduction to planktonic thin layers and the LOCO project. *Continental Shelf Research* **30** (1), 1–6.

Turner, J. T. 2002 Zooplankton fecal pellets, marine snow and sinking phytoplankton blooms. *Aquatic Microbial Ecology* **27** (1), 57–102.

White, F. M. 1974 *Viscous fluid flow*. McGraw-Hill, New York.

Yick, K. Y., Torres, C. R., Peacock, T. & Stocker, R. 2009 Enhanced drag of a sphere settling in a stratified fluid at small Reynolds numbers. *Journal of Fluid Mechanics* **632** (-1), 49–68.